



The Canadian Atmospheric Model version 5 (CanAM5.0.3)

Jason Neil Steven Cole¹, Knut von Salzen¹, Jiangnan Li¹, John Scinocca¹, David Plummer¹, Vivek Arora¹, Norman McFarlane¹, Michael Lazare¹, Murray MacKay², and Diana Verseghy³

¹Canadian Centre for Climate Modelling and Analysis, Environment and Climate Change Canada, Victoria, British Columbia, Canada

²Environmental Numerical Weather Prediction Research Section, Environment and Climate Change Canada, Toronto, Ontario, Canada

³Climate Processes Section, Environment and Climate Change Canada, Toronto, Ontario, Canada

Correspondence: Jason Neil Steven Cole (jason.cole@ec.gc.ca)

Received: 29 January 2023 – Discussion started: 7 February 2023

Revised: 11 May 2023 – Accepted: 5 August 2023 – Published: 22 September 2023

Abstract. The Canadian Atmospheric Model version 5 (CanAM5) is the component of Canadian Earth System Model version 5 (CanESM5) which models atmospheric processes and coupling of the atmosphere with land and lake models. Described in this paper are the main features of CanAM5, with a focus on changes relative to the last major scientific version of the model (CanAM4). These changes are mostly related to improvements in radiative transfer, clouds, and aerosol parameterizations, as well as a major upgrade of the land surface and land carbon cycle models and addition of a small lake model. In addition to changes to parameterizations and models, changes in the adjustable parameters between CanAM4 and CanAM5 are documented. Finally, the mean climatology simulated by CanAM5 for the present day is evaluated against observations and compared with that simulated by CanAM4. Although many of the aspects of the simulated climate are similar between CanAM4 and CanAM5, there is a reduction in precipitation and temperature biases over the Amazonian basin, global cloud fraction biases, and solar and thermal cloud radiative effects, all of which are improvements relative to observations.

1 Introduction

The fifth version of the Canadian Atmospheric Model (CanAM5; for a list of acronyms, initialisms, and abbreviations, see Table A3) is a major component model in the Canadian Earth System Model version 5 (CanESM5) (Swart

et al., 2019), modelling atmospheric processes and coupling of the atmosphere with land and lake models. Both CanAM5 and CanESM5 are models developed by the Canadian Centre for Climate Modelling and Analysis (CCCma) to simulate climate to improve understanding and make predictions and projections of future climate. CanAM5 is the result of several years of development on its last major scientific version, CanAM4 (von Salzen et al., 2013), which was the atmospheric component of CanESM2 (Arora et al., 2011) used for the fifth Coupled Model Intercomparison Project (CMIP5) (Taylor et al., 2011). Between CanAM4 and CanAM5, there were numerous changes to radiative transfer, cloud, and aerosol parameterizations, in addition to a major upgrade of the land surface model and addition of a model of unresolved subgrid-scale lakes.

CanESM5 and CanAM5 were the basis for CCCma's contribution to CMIP6 (Eyring et al., 2016), which included a number of experiments to better understand and characterize cloud feedbacks and radiative forcings. The mean state and response of CanESM5 to external forcing in fully coupled simulations are documented in Swart et al. (2019). In this paper, the focus is on the ability of CanAM5 to simulate the historical climate for simulations in which sea surface temperature and sea ice concentration are prescribed from observations. Since there are several changes in CanAM5 relative to CanAM4, most of the evaluation with observations is performed with both CanAM5 and CanAM4 to highlight changes in the simulated climate.

In Sects. 2 and 3, changes in atmospheric and surface processes between CanAM4 and CanAM5 are summarized. The

process used to tune CanAM5 is discussed in Sect. 4, and the values used for adjustable parameters are presented. The details of experiments used to evaluate CanAM5 are presented in Sect. 5, and Sect. 6 presents an analysis of climatological features of CanAM5. Finally, in Sect. 7, we conclude with a brief summary and discussion of the main results of this study.

2 Atmospheric processes

This section summarizes atmospheric parameterizations in CanAM5. As most parameterizations are described and documented in detail for CanAM4 (von Salzen et al., 2013) we focus on the major changes between CanAM5 and CanAM4.

The horizontal resolution of CanAM5 is identical to CanAM4 and is defined by triangular truncation at a total wavenumber of 63 (i.e., T63). The model employs a double spectral transform allowing the physical tendencies to be evaluated on a reduced “linear” T63 Gaussian grid of dimensions 128×64 , which corresponds to $\sim 2.8^\circ$. The number of vertical levels in CanAM5 has increased from 35 to 49. The 49 levels are used with layer thicknesses that increase monotonically from approximately 100 m at the surface to 2 km at ~ 1 hPa, which is the upper bound of the vertical domain. The additional 14 layers in CanAM5 have been added to the upper troposphere and lower stratosphere to match those employed by the Canadian Middle Atmosphere Model (Scinocca et al., 2008).

2.1 Radiation

Radiative transfer in CanAM5 includes the new specification of optical properties for the surface, cloud, and aerosol, in addition to the computation of radiative fluxes accounting for subgrid-scale surface variability.

The parameterized absorption by gases uses a correlated k -distribution model that is mostly unchanged from CanAM4, using the same wavelength intervals and quadrature points (von Salzen et al., 2013). A significant modification is the addition of a solar water vapour continuum (Mlawer et al., 1997), which resulted in improved simulation of absorption at solar wavelengths (Pincus et al., 2015). The single-scattering properties of the ice clouds in CanAM4 were parameterized for thermal and solar wavelengths under the assumption that all the ice particles are hexagonal prisms (von Salzen et al., 2013). In CanAM5 the optical properties of ice particles use the parameterization of Yang et al. (2012), assuming a mixture of ice habits that is based on spaceborne observations and assuming a moderately rough surface, which is found to improve retrievals (Baum et al., 2011). The single-scattering properties of pure liquid clouds remain the same but can be perturbed to account for internally mixed black carbon (Li et al., 2013), allowing simulation of the semi-indirect effect.

Aerosol optical properties in CanAM5 use updated single-scattering properties as well as an improved method to mix aerosol optics. The single-scattering properties for organic carbon use the refractive index from HITRAN 2012 (Rothman et al., 2013) and the properties of black carbon from Flanner et al. (2012). Instead of externally mixing aerosols, it is assumed that sulfate and the hydrophilic components of black carbon and organic carbon are internally mixed (Wu et al., 2018). The refractive index of the internally mixed aerosol is computed based on the fraction, effective radius, and effective variance of each component aerosol, as well as relative humidity, which is used to compute hydrophilic growth.

The ocean optical properties are also changed in CanAM5. In CanAM4, the whitecap albedo was wavelength-invariant with a value of 0.3. In CanAM5, each wavelength interval in the solar radiative transfer model uses a different albedo (0.216, 0.134, 0.044, 0.005) based on Frouin et al. (2001). The parameterization of ocean albedo is similar to that in CanAM4, but the contents of the lookup table have been updated and now include a dependence on the solar zenith angle and partitioning of the incident downwelling solar radiation into direct and diffuse components (Jin et al., 2011). This partitioning is estimated using the vertically integrated aerosol and cloud optical depth. In CanAM4, the ocean albedo was computed using as input optical thickness and solar zenith angles from the last radiative transfer time step, which is 1 h earlier. To improve the consistency of the ocean albedo calculation and the radiative transfer calculations, especially near sunrise and sunset, in CanAM5 the ocean albedo is calculated using cloud and aerosol information from the previous dynamical time step, 15 min earlier, and the solar zenith angle from the current time step.

Over land, the dry bare-soil albedo in CanAM4 was set to a global constant combined with a parameterization to account for the effect of surface wetting (Verseghy, 2012). The use of a globally constant bare-soil albedo resulted in regional biases for clear-sky albedo at the top of atmosphere, especially over the Sahara and Australian interior. The constant albedo was replaced with a regionally varying soil colormap and associated albedos (Lawrence and Chase, 2007). These new location-dependent bare-soil albedo maps greatly reduced biases in clear-sky albedo relative to observations. In addition to the bare soil, the albedo and emissivity of snow and sea ice were also updated. The albedo of snow on land and sea ice in CanAM5 is computed using a lookup table accounting for snowpack properties. These include snow water equivalent, snow grain size, and black carbon simulated by the land surface model (Namazi et al., 2015). Snow present on land or sea ice uses a single, wavelength-invariant emissivity, which was reduced from 1.0 to 0.97 (Chen et al., 2014). Similarly, the emissivity of sea ice was reduced from 1.0 to 0.97 to be consistent with the sea ice model used in CanESM5 (Fichefet and Maqueda, 1997).

Within a CanAM5 grid box, there can be multiple surface types including land, lake, ocean, and sea ice (Sect. 3.3). When coupling the atmosphere with ocean, sea ice, and land models, it is necessary to have surface radiative fluxes that are consistent with each surface type. While it is possible to partition the grid-mean radiative fluxes at the surface using the tiled albedo, emissivity, and temperature, in CanAM5 radiative flux profiles are instead computed for each surface type and then averaged to a grid mean. It is assumed that the same atmosphere is present over each tile. Although this approach causes a small increase (< 5 %) in the total time for global radiative transfer calculations in CanAM5, it maintains consistency between the surface and the atmosphere. The modest increase in computational time is possible because multiple surface tiles are only present in a portion of the CanAM5 grid boxes, e.g., there is only one surface type over sea-ice-free ocean.

2.2 Aerosols and chemistry

The types of natural and anthropogenic aerosols in CanAM5 include sulfate, black and organic carbon, sea salt, and mineral dust, similar to CanAM4 (von Salzen et al., 2013). Parameterizations for aerosol emissions and transport, gas-phase and aqueous-phase chemistry, and dry and wet deposition account for interactions with simulated meteorology. Natural aerosol species are represented in the model using prognostic emission fluxes. In particular, a particle-size-dependent emission scheme is used to account for aeolian erosion in arid and semi-arid regions (Peng et al., 2012). Sea salt concentrations in two size modes are parameterized as a function of the wind speed near the surface of the ocean (Ma et al., 2008). Dimethyl sulfide emissions are predicted using specified climatological concentrations in the surface ocean (Tesdal et al., 2016a, b). Sulfur oxidation in the gas and aqueous phases is simulated using specified climatological oxidant concentrations from CMAM20 (McLandsess et al., 2013).

The chemistry parameterizations in CanAM5 are unchanged relative to CanAM4 with the exception of stratospheric water vapour which can be produced by methane oxidation using a parameterization based on that described in ECMWF (2003).

2.3 Clouds

The parameterization of clouds and cloud microphysics in CanAM5 is mostly the same as in CanAM4 (von Salzen et al., 2013). Like CanAM4 and other global climate models, CanAM5 continues to employ bulk cloud microphysical parameterizations which depend on mean water content and other moments of the droplet size distribution.

Autoconversion in liquid clouds is parameterized in CanAM4 using Khairoutdinov and Kogan (2000), but this has been replaced in CanAM5 with the autoconversion pa-

rameterization of Wood (2005), which is a modified version of the parameterization by Liu and Daum (2004), to simulate the collision and coalescence of cloud droplets. For convenience we reproduce here the main equations for Khairoutdinov and Kogan (2000) and Wood (2005), since the adjustment of parameters in the equations is discussed in Sect. 4.

Autoconversion in CanAM4 is parameterized as (Khairoutdinov and Kogan, 2000)

$$\frac{\partial q_r}{\partial t} = A \overline{q_L^{2.47}} N_d^{-1.79} \rho^{-1.47}, \quad (1)$$

where A is a constant, q_r is the rainwater content (in kg m^{-3}), q_L is the liquid cloud water content (in kg m^{-3}), N_d is the cloud droplet number concentration (in m^{-3}), and ρ is air density (in kg m^{-3}). In CanAM5, the autoconversion is parameterized as (Wood, 2005)

$$\frac{\partial q_r}{\partial t} = E \overline{q_L^3} N_d^{-1} H(R_6 - R_{6C}), \quad (2)$$

where q_r is the rainwater content (in kg m^{-3}), q_L is the liquid cloud water content (in kg m^{-3}), N_d is the droplet number concentration (in m^{-3}), and $H()$ is the Heaviside function. Additionally, $E = 1.3 \times 10^9 \beta_6^6$, $R_{6C} = 7.5 / (\overline{q_L}^{1/6} R_6^{1/2})$, $R_6 = \beta_6 r_v$, and $\beta_6 = [(r_v + 3) / r_v]$, where r_v is the mean volume radius (in μm). In order to account for the impacts of subgrid-scale variability in cloud liquid water content, the statistical cloud scheme in CanAM5 (von Salzen et al., 2013) is used to determine the mean value of q_L^3 , indicated by the bar in Eq. (2).

Along with the new autoconversion parameterization, CanAM5 now accounts for indirect impacts of aerosols on cloud liquid water content and lifetime, i.e., the second aerosol indirect effect (Ghan et al., 2013). This effect was not active in CanAM4, since it used a constant cloud droplet number concentration of 50 cm^{-3} in Eq. (1) (von Salzen et al., 2013). Given the uncertainty of applying the parameterizations at high altitudes, cloud processes are limited to pressures greater than 10 hPa.

3 Surface processes

There were three substantial changes to the treatment of surface processes: a major upgrade of the land surface including tighter integration of the land carbon cycle model, a small lake model, and tiling to accommodate fractional land in a grid box.

3.1 CLASS-CTEM

The land component of CanAM5 is represented by the Canadian Land Surface Scheme (CLASS) and the Canadian Terrestrial Ecosystem Model (CTEM), which model physical and biogeochemical processes, respectively. CanAM5 uses version 3.6 of CLASS, which models the energy and moisture fluxes at the air–land surface interface (Verseghy, 2012).

Compared to its predecessor used in CanAM4 (CLASS 2.7; Verseghy, 1991; Verseghy et al., 1993) there are several major structural improvements in version 3.6 of CLASS. These include optional implementation of a user-specified number of soil layers rather than the previous hard-coded three layers, as well as the capability of supporting a mosaic of vegetation, soil, water, or ice tiles within grid cells. The capability of modelling fully organic soils has been introduced, with hydraulic properties assigned on the basis of the work of Letts et al. (2000). The thermal conductivities of the organic and mineral soil layers are determined following Côté and Konrad (2005) and Zhang et al. (2008). The wet and dry albedos of the mineral soil are assigned based on a global soil reflectivity index described in Lawrence and Chase (2007) and Oleson et al. (2010). Organic soil albedos are assigned following Comer et al. (2000). The bare-soil surface evaporation efficiency parameter is calculated using a relation presented by Lee and Pielke (1992). Empirical corrections are applied to the saturated hydraulic conductivity of each soil layer to take into account the viscosity of water at the layer temperature (Dingman, S., L., 2002) and the presence of ice (Zhao and Gray, 1997). The field capacity of the lowest permeable soil layer and the baseflow at the bottom of the layer are obtained using relations derived from Soulis et al. (2011).

A new option is provided to model snowpack albedo and transmissivity in four wavelength intervals instead of two intervals. The thermal conductivity of snow is obtained from the snow density using a relationship derived by Sturm et al. (1997). The fresh snow density is calculated as an empirical function of the air temperature, using relations developed by Hedstrom and Pomeroy (1998) and Pomeroy and Gray (1995). The maximum snowpack density is calculated as a function of snow depth following Tabler et al. (1990). The amount of snowfall intercepted by vegetation and the unloading rate of intercepted snow are calculated following Hedstrom and Pomeroy (1998). The canopy interception capacity for snow is determined from the plant area index and the fresh snow density as described in Bartlett et al. (2006) and Schmidt and Gluns (1991). Albedos of snow-covered vegetation canopies are set following Bartlett and Verseghy (2015). The sensible and latent heat fluxes between the vegetation, the underlying ground, and the overlying atmosphere are evaluated based on the analysis of Garratt (1992), which incorporates an explicit treatment of the canopy air space.

Although CLASS 3.6 can represent vegetation as a mosaic, the composite approach of representing different vegetation types in a grid cell is employed in CanAM5. This implies that area-weighted grid-mean structural attributes of different vegetation types are used in energy and water balance calculations. The number of soil and bedrock layers remains three, the same as in CanAM4, with the first and second soil layers being 0.1 and 0.25 m thick. The maximum thickness of the permeable soil for the third layer is 3.75 m

but varies geographically depending on the permeable soil depth specified following Zobler (1986).

CTEM models vegetation as a dynamic component of the climate system and provides structural attributes of vegetation to CLASS for use in its physics calculations (Arora and Boer, 2005). These include leaf area index, vegetation height, rooting depth and distribution, and canopy mass. The biogeochemical component CTEM has not changed much from CanAM4 except the diagnostic calculation of wetland extent and methane emissions (Arora et al., 2018), none of which affects the physical land surface processes.

3.2 Canadian Small Lake Model

CanAM5 includes a parameterization for subgrid-scale lakes to improve surface fluxes of heat and moisture over land masses. The scheme is based on the Canadian Small Lake Model, CSLM (MacKay, 2012; MacKay et al., 2017). This scheme computes a nonlinear surface energy balance in a thin skin layer and then solves the heat equation based on thermal conduction and shortwave radiation extinction following Beer's law for both visible and near-infrared bands. A diurnal surface mixed layer is simulated based on the bulk turbulent kinetic energy approach, e.g., Niiler and Kraus (1977), developed by Rayner (1980), Imberger (1985), and Spigel et al. (1986) for lakes. A seasonal thermocline arises naturally as a result of the daily excursions of the surface mixed layer. The equation of state follows Farmer and Carmack (1981), except that the effects of pressure and salinity are neglected.

The model allows for the formation of both black, i.e., congelation, and white ice. Black ice forms when the energy balance in a layer is sufficiently negative to cool it below 0 °C. White ice forms when the weight of the overlying snowpack is sufficient to crack the ice and allow lake water to flood a layer of snow, which is then assumed to freeze immediately and completely. Latent heat from the freezing of the pore water is first used to warm the snow crystals in the slush layer to 0 °C, with the remainder going into the overlying snowpack. Both white and congelation ice is assumed to be free of air bubbles and to have the same transmissivity.

Fractional ice cover, following Leppäranta and Wang (2008), and fractional snow on ice are permitted, thus allowing for the simultaneous presence of open water, bare ice, and snow-covered ice. Fractional ice cover is especially important for larger lakes subject to sufficient wind stress, which can mechanically break ice to produce pressure ridges and open water leads. The presence of some open water will alter turbulent and radiative flux exchange with the atmosphere, as well as light availability at depth due to differences in roughness, albedo, and light extinction between water and ice. Snow itself is represented as in the Canadian Land Surface Scheme (CLASS; Sect. 3.1), with the snowpack simulated as a layer thermally distinct from the underlying ice.

The properties and interaction of all lakes within a CanAM5 grid cell are modelled by one representative sub-

grid lake using CSLM. The properties of the representative lake in each CanAM5 grid cell are derived from the Global Lake Database version 2 (GLDv2) (Kourzeneva et al., 2012; Choulga et al., 2014), which is provided at $1/120^\circ \times 1/120^\circ$ resolution. The grid fraction covered by the representative lakes is derived from the aggregate area of lakes in GLDv2 that falls within each CanAM5 grid cell. This defines the unresolved lake tile (Sect. 3.3). Lake dynamics are governed by three external geophysical parameters that must be specified: the visible light transparency, mean depth (or volume), and mean fetch. For all representative lakes, a constant transparency of 0.5 m^{-1} is assumed and the mean depth and mean fetch in each CanAM5 grid cell are derived in an aggregate manner from GLDv2.

3.3 Tiling

To more easily facilitate conservative coupling, all previous versions of coupled atmosphere–ocean models developed at CCCma employed coincident grids with an identical binary land mask; e.g., CanESM2 employed CanAM4’s land mask for its CMIP5 contribution. In these earlier versions, enhanced ocean resolution was achieved by prescribing multiple ocean grid cells below each CanAM atmospheric grid cell. For CanESM5, independent arbitrarily oriented grids are assumed for both the atmosphere and the ocean (Swart et al., 2019). This required the implementation of a fractional land mask in the atmospheric model and tiling of its underlying surface. In general, each CanAM5 grid cell can contain tiles representing land, ocean, sea ice, and unresolved lakes. The tiling approach used is a generalization of that discussed in Sect. 3.1 for the tiling of vegetation types over the land portion of atmospheric grid cells. For example, within each model grid cell, independent energy and water fluxes are derived over each underlying surface type given its unique properties, e.g., temperature and albedo. On the atmospheric side, these fluxes undergo a weighted aggregation based on the tile fraction to produce a single flux seen by the atmosphere. In fully coupled mode, if ocean and/or sea ice sits below some portion of an atmospheric grid cell, the flux of each representing each surface type is passed to the coupler, CanCPL, and is remapped and transferred to the underlying grid of the ocean and/or sea ice model.

Currently, surface tiling in CanAM5 has been implemented for the parameterization of radiative transfer, surface processes, and vertical diffusion. Aside from the radiation, the fluxes over each tile are derived from the prognostic variables in the lowest model level, e.g., temperature, specific humidity, and wind. For simplicity, the blending height at which the fluxes from each tile are aggregated is also taken to occur in the lowest atmospheric model level. For radiative transfer calculations, profiles of radiative fluxes are computed for each of the tiles and aggregated into a grid mean, while fluxes are maintained for each tile as described in Sect. 2.1.

3.4 Snow on sea ice

For snow on sea ice in CanAM5, the parameterization of snow cover fraction was updated and a parameterization of wet-snow grain growth added to improve consistency with the treatment of snow on land.

In CanAM4, different parameterizations of snow cover were used on land and on sea ice, the snow cover on land being (Verseghy, 2012)

$$X_{\text{snow}} = \begin{cases} Z_{\text{snow}}/Z_{\text{snow,lim}} & \text{if } Z_{\text{snow}} \leq Z_{\text{snow,lim}} \\ 1.0 & \text{if } Z_{\text{snow}} > Z_{\text{snow,lim}} \end{cases} \quad (3)$$

and snow cover over sea ice being

$$X_{\text{snow}} = \begin{cases} \sqrt{\text{SWE}/\text{SWE}_{\text{lim}}} & \text{if } \text{SWE} \leq \text{SWE}_{\text{lim}} \\ 1.0 & \text{if } \text{SWE} > \text{SWE}_{\text{lim}} \end{cases}, \quad (4)$$

where X_{snow} is the fractional area of the land or sea ice covered with snow, Z_{snow} is the depth of the snow (in m), and SWE is the snow water equivalent (in kg m^{-2}), with $Z_{\text{snow,lim}}$ and SWE_{lim} being adjustable limits for each. In CanAM5, Eq. (3) is used to determine snow cover over land and sea ice. Note that in Eq. (3), Z_{snow} is initially computed using $Z_{\text{snow}} = \text{SWE}/\rho_{\text{snow}}$, where ρ_{snow} is the snow density (in kg m^{-3}). If $Z_{\text{snow}} \leq Z_{\text{snow,lim}}$, then $Z_{\text{snow}} = Z_{\text{snow,lim}}$ and the SWE is adjusted accordingly (Verseghy, 2012).

The computation of sea ice albedo includes a contribution from snowpack on sea ice when it is present. To calculate the albedo of snow, it is necessary to simulate the relevant physical properties of the snow, including the snow grain size. The approach used to parameterize these properties in CanAM5 is described in Namazi et al. (2015). Described here is the addition of a parameterization to CanAM5 so that the wet growth of snow grains is included for snow on sea ice, where previously only the dry growth of snow grains was considered.

To calculate the wet growth of snow grains, the same expression is used as over land (Eq. 3 of Namazi et al., 2015), which requires the liquid water fraction in the snowpack. This was not available in CanAM5, so we added a parameterization of snowpack liquid water fraction using Anderson (1976):

$$F_{\text{liq}} = \begin{cases} F_{\text{liq,min}} & \text{if } \rho_{\text{snow}} \geq \rho_{\text{snow,thres}} \\ F_{\text{liq,min}} + \Delta F_{\text{liq}} & \text{if } \rho_{\text{snow}} < \rho_{\text{snow,thres}} \end{cases}, \quad (5)$$

where F_{liq} is the fraction of liquid in the snow pack, ρ_{snow} is the density of snow (in kg m^{-3}), and $\rho_{\text{snow,thres}}$ is the snow density threshold at which $F_{\text{liq,min}}$ occurs. The term ΔF_{liq} is $(F_{\text{liq,max}} - F_{\text{liq,min}}) \times \frac{\rho_{\text{snow,thres}} - \rho_{\text{snow}}}{\rho_{\text{snow,thres}}}$, where $F_{\text{liq,max}}$ and $F_{\text{liq,min}}$ are the maximum and minimum allowed values of F_{liq} .

4 Setting adjustable parameters

After finalizing the new and updated physical parameterizations, they were no longer changed, except for a subset of adjustable parameters. These parameters were manually adjusted within a range of physically plausible values to obtain an acceptable preindustrial climate in the coupled atmosphere–ocean configuration of CanESM5 (Swart et al., 2019). This is the last exercise performed to finalize a model version and is often referred to as “tuning”. The subset of parameters and values in CanAM5 is provided in Table 1. They include parameters adjusted specifically for CanAM5 and parameters adjusted when tuning intermediate versions of CanAM between versions 4 and 5, e.g., CanAM4.1. In this section, we discuss the process used to arrive at the values, which is different from that used in CanAM4 and CanESM2.

The tuning of CanESM2 was carried out mainly by adjusting the parameters of each of its components separately, including CanAM4, with a goal of minimal additional adjustments when fully coupled. For example, the parameters for CanAM4 were mostly tuned using transient prescribed sea surface temperature (SST) and sea ice simulations of the near present, consistent with simulations used regularly for CanAM development. Applying the same approach to the tuning of CanESM5 resulted in a coupled preindustrial (1850) control simulation with a climate that was too cold with excessive sea ice relative to observations. Therefore, CanAM5 was tuned in the context of fully coupled CanESM5 simulations, with a particular focus on obtaining preindustrial control conditions with global mean temperatures and sea ice within acceptable ranges. The combination of parameters that achieved this target was then evaluated to verify that other aspects of the climate remained acceptable.

Analyses to investigate the effect of parameter sets on the climate included CanAM5 simulations using prescribed SSTs and sea ice (Atmospheric Model Intercomparison Project, AMIP; Eyring et al., 2016). For the most part, the mean climate simulated in AMIP mode was close to coupled CanESM5 simulations with the exception of the net radiative flux at the top of atmosphere (TOA). Adjustments required to ensure an acceptable preindustrial climate resulted in a net downward flux at TOA ($\sim 3.1 \text{ W m}^{-2}$) in historical AMIP runs, which is larger than observations. Simulations in which the AMIP net downward fluxes at TOA were close to those observed resulted in a preindustrial global mean temperature up to 2K colder than the target value. Although the AMIP net downward fluxes at TOA are larger than those observed, their value in CanESM5 historical coupled simulations during the present day are very close to observations ($\sim 1 \text{ W m}^{-2}$; Fig. S6). Details of the TOA radiative fluxes are discussed in Sect. 2.1. For the purposes of tuning, this particular bias in AMIP simulations was retained to get a reasonable preindustrial control climate.

Table 1 lists parameters that changed between CanAM4 and CanAM5, with those in bold specifically adjusted for

CanAM5 and others having been changed when tuning intermediate CanAM versions between CanAM4 and CanAM5. This table does not include parameters that were adjusted in the ocean or in the sea ice model that only affected coupled simulations. The rightmost column of Table 1 provides sources and, where possible, references that explain the setting in CanAM. This final set of CanAM5 parameters allows us to simulate a climate that is on balance reasonable relative to observations in both coupled and AMIP mode.

The parameters related to cloud microphysics have notable effects on radiative energy budgets and coupled climate, including emergent CanESM5 properties such as climate sensitivity. Of particular importance are the two parameters scaling the efficiency of cloud droplet autoconversion and accretion to precipitation. In CanAM5, the accretion rate factor was the main parameter adjusted instead of autoconversion, which is opposite to the approach used when tuning CanAM4. Analysis of satellite observations by Lebsock et al. (2013) indicates global climate models may severely underestimate mean accretion rates when subgrid cloud–precipitation covariability is omitted. Furthermore, Gettelman et al. (2015), Sant et al. (2015), and Michibata et al. (2019) showed that diagnostic parameterizations of rain processes, such as those employed in CanAM5, produce considerably lower accretion rates than prognostic and more comprehensive parameterizations. Consequently, the usual assumptions of an instantaneous and horizontally uniform precipitation flux in the cloudy portions of the grid cells in CanAM5 likely cause unrealistically low accretion rates. In an attempt to compensate for this, the original parameterization of accretion of Khairoutdinov and Kogan (2000) is made more efficient through the considerable increase (by a factor of 15) in the tunable parameter. Autoconversion rates, on the other hand, are not scaled.

5 Control and CMIP6 simulations

Unlike CanAM4, CanAM5 has an interactive land carbon cycle (Sect. 3.1) which necessitates starting CanAM5 transient simulations from a state with a land carbon cycle that is reasonably close to equilibrium. To achieve this, sufficiently long simulations with a stable climate are required. This is done using an approach similar to the spinup of the CanESM5 preindustrial simulation (Swart et al., 2019). A long control simulation of CanAM5 is performed using a repeating annual cycle of forcing and prescribed sea surface temperature (SST) and sea ice. For this CanAM5 control, we use forcing for the year 1870 (the first year in the historical SST and sea ice dataset), while the annual cycle of SST and sea ice is the mean over 1870–1879.

With this configuration, the CanAM5 control simulation was initialized from a coupled CanESM5 1850 control simulation and run for ~ 300 years until the physical and biogeochemical land states, including carbon in vegetation and

Table 1. Adjustable parameters in CanAM and their settings in CanAM5. The values in bold were specifically tuned in CanAM5, while the others were used to tune intermediate versions of CanAM. The rightmost column indicates references that discuss the adjustable parameter or include further references about the parameter.

Scheme	Parameter	Physical description	CanAM5	Unit	Comment/reference
Cloud microphysics	facacc	Factor scaling mass accretion rate of cloud water to precipitation due to the collection of cloud droplets by rain-drops	15	–	Wood (2005)
	facaut	Factor scaling efficiency coefficient in mass autoconversion rate of cloud water to precipitation due to the collision–coalescence processes of cloud droplets	1	–	Khairoutdinov and Kogan (2000)
	uicefac	Prefactor in power law describing ice crystal fall speed due to the influence of gravity	6000	s ^{−1}	von Salzen et al. (2013)
Moist convection	alf	Proportionality parameter relating vertically integrated convective kinetic energy with the cloud base mass flux	5.0 × 10 ⁸	m ⁴ kg ^{−1}	Scinocca et al. (2008)
	ccu	Weight large-scale and pressure gradient force contributions to moist convection horizontal velocity (updrafts)	0.0	–	von Salzen et al. (2013)
	ccd	Weight large-scale and pressure gradient force contributions to moist convection horizontal velocity (downdrafts)	0.0	–	von Salzen et al. (2013)
Gravity wave	fcrit	Critical inverse Froude number	0.22	–	
	gphil	Mountain sharpness number	1.0	–	Scinocca and McFarlane (2000)
Vertical diffusion	rkhmn	Minimum background vertical diffusivity for temperature	0.1	m ² s ^{−1}	von Salzen et al. (2013)
	rkqmn	Minimum background vertical diffusivity for moisture	0.1	m ² s ^{−1}	von Salzen et al. (2013)
Surface processes	drn	Scaling factor for soil drainage at the bottom of the soil levels	0.1	–	Verseghy (2012)
	cuscale	Scaling factor of the wind stress threshold for dust emissions	1.6	–	Peng et al. (2012)
	reff0_sea	Background specific surface area of snow grains (on sea ice)	30	m ² kg	Personal communication (Joshua King)
	reff0_land	Background specific surface area of snow grains (on land)	60	m ² kg	Personal communication (Joshua King)
	albp	Depth of melt ponds on sea ice	20	cm	Ebert and Curry (1993)

soil, approached a new quasi-equilibrium. The simulation was then extended by an additional 200 years. Figure 1 shows the net atmosphere–land CO₂ flux, the amount of C in the soil carbon pool, and the total soil moisture during the 200 years. Most atmospheric variables reached a quasi-equilibrium within a few years and are therefore not shown. For CanESM5, transient coupled simulations were started from the control coupled simulation every 50 years (Swart

et al., 2019). A similar approach was used for CanAM5 with transient simulations starting from the CanAM5 control simulation every 10 years beginning at the year 400. These are used to generate a 10-member ensemble using transient forcings, SSTs, and sea ice for the period 1870 to 2014.

Several CMIP6 experiments were performed using CanAM5 and prescribed SSTs and sea ice. The 10-member ensemble of 1870–2014 transient simulations was con-

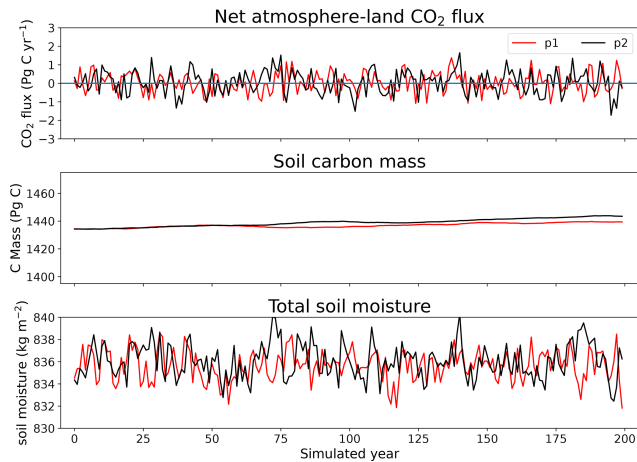


Figure 1. Net atmosphere–land CO_2 flux (Pg C yr^{-1}), soil carbon mass (Pg C), and total soil moisture (kg m^{-2}) for the years 300–500 of the CanAM5 1870 control simulation. The red and black lines show the results for CanAM5 using two different physics configurations of CanESM5, p1 and p2, respectively, the details of which are described in Swart et al. (2019).

tributed to the Global Monsoon Model Intercomparison Project (Zhou et al., 2016), while the period 1950 to 2014 from each simulation makes up the CanESM5 contribution to the Atmospheric Model Intercomparison Project (AMIP) experiments (Eyring et al., 2016). AMIP simulations are the basis for several Cloud Feedback Model Intercomparison Project (CFMIP) experiments used to characterize and understand cloud feedbacks (Webb et al., 2017). To characterize radiative forcings in CanESM5, simulations were performed using the Radiative Forcing Model Intercomparison Project (RFMIP) protocols for time slice and transient historical forcings (Pincus et al., 2016), which are summarized in Smith et al. (2020).

6 Evaluation of CanAM5 climatology

The properties of coupled atmosphere–ocean experiments using CanESM5 are shown in Swart et al. (2019). Documented in this section is the climatology of CanAM5 from the CMIP6 AMIP simulation, evaluated against observations and highlighting differences compared to CanAM4 from a CMIP5 AMIP simulation. Details of observations used for evaluation are summarized in Table A1, and model variables are summarized in Table A2. For all figures, the first ensemble member is used for each AMIP simulation, r1i1p1 for CanAM4 and r1i1p2f1 for CanAM5. Included in several figures is the global, or near-global, mean bias, root mean square error, and Pearson correlation coefficient between the time-averaged CanAM and observations. For the most part, the results using prescribed SSTs and sea ice are similar to coupled CanESM5 and CanESM2 simulations. For ease of comparison with CanESM5 coupled simulations (Swart

et al., 2019), the figures in this section have been reproduced in the Supplement, Sect. S2, using the first member (r1i1p2f1) of the CanESM5 historical simulation ensemble.

6.1 Clouds and precipitation

The near-global (equatorward of 60°) cloud fraction as a function of cloud optical thickness and cloud top pressure is shown in Fig. 2. For the purposes of comparing more consistent model output from CanAM5 and CanAM4 with observations, output from the International Satellite Cloud Climatology Project (ISCCP) simulator (Bodas-Salcedo et al., 2011) is compared with ISCCP observations, both ISCCP-D (Rossow and Schiffer, 1999) and ISCCP-H (Knapp et al., 2021). The two versions of ISCCP observations are used to illustrate the uncertainty in the cloud properties, an uncertainty that only increases once other cloud observations are considered (Stubenrauch et al., 2013). For example, Pincus et al. (2015) showed that there are large differences between ISCCP and MODIS (larger than between the two versions of ISCCP shown here). Therefore, it is important that such differences be considered in the evaluation of models, especially for optically thin clouds.

With these caveats in mind, the histograms of biases indicate that CanAM5 generally simulates too much cloud with moderate optical thickness of high- and low-altitude clouds and simulates too little cloud at mid-level altitudes. Summing the histograms over cloud top pressure to look at clouds as a function of visible optical thickness, we see that there are more optically thin ($\tau < 23$) clouds in CanAM5 than in CanAM4. The structure of these biases relative to ISCCP is consistent with previous studies, for example Klein et al. (2013).

The zonal mean structure for cloud amount is presented (Fig. 3), which illustrates that the near-global mean biases are the result of regional biases which are a source of biases and improvements in the cloud radiative effect (CRE) (Fig. 7). As seen in the near-global means, the differences between ISCCP-D and ISCCP-H are smaller than biases between CanAM and ISCCP-H and the change in biases between CanAM4 and CanAM5. Although there remain biases in the total cloud amount, there is a systematic reduction in biases in CanAM5 by $\sim 3.4\%$ in the near-global mean compared to biases in CanAM4. Parsing the biases in CanAM5 by the altitude of cloud top pressure, the increase in the CanAM5 total cloud amount mostly is caused by increased non-low (cloud top pressure < 680 hPa) cloud amount. From CanAM4 to CanAM5, there is an increase in the amount of “thin” (cloud visible τ between 0.3 and 23) and reduction in “thick” (cloud visible $\tau > 23$) cloud at all latitudes, consistent with the near-global mean (Fig. 2). This increase in cloud amounts is consistent with the change in CREs (Fig. 7). The shift to more optically thin cloud would reduce the reflectivity, doing so in a nonlinear manner, while the increase in

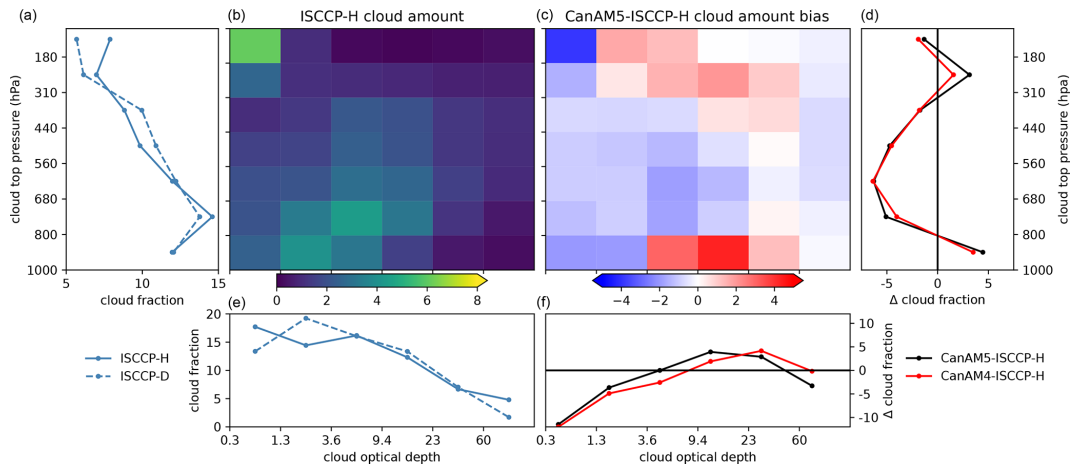


Figure 2. Mean histograms of the cloud fraction equatorward of 60° as a function of the cloud top pressure and cloud visible optical thickness from ISCCP-H and the biases in CanAM5 (b, c). To the side of each histogram is the mean cloud fraction, or cloud fraction bias, as a function of cloud top pressure, while below each histogram the cloud fraction is shown, or cloud fraction bias, as a function of cloud optical thickness. Means are averages for 1987–2008.

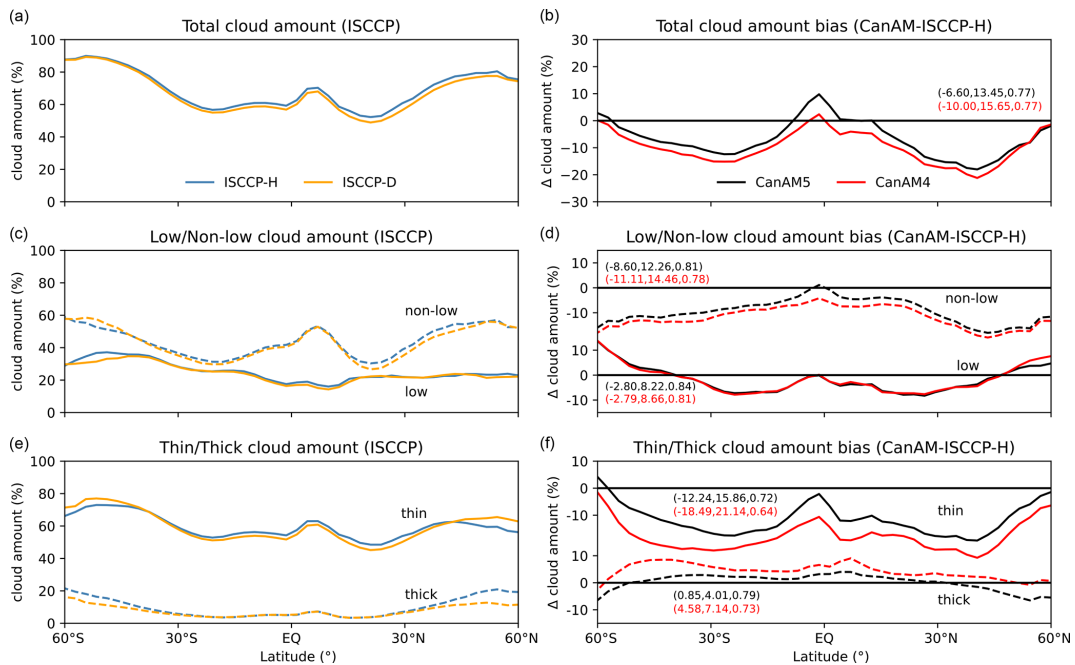


Figure 3. Zonal mean cloud fraction for the total cloud amount with $\tau > 0.3$ (a, b), cloud amount for low (cloud top pressure > 680 hPa) and non-low (cloud top pressure < 680 hPa) in (c) and (d), and the cloud amount for thin (cloud visible τ between 0.3 and 23) and thick (cloud visible $\tau > 23$) in (e) and (f). Observations for ISCCP-H and ISCCP-D are shown in (a), (c), and (e) and biases for CanAM5 and CanAM4 relative to ISCCP-H in (b), (d), and (f). Bracketed numbers in (b), (d), and (f) are, in order, mean bias, root mean square error, and Pearson correlation coefficient, computed over the period 1987–2008 and from 60° S to 60° N, with black font for CanAM5 and red font for CanAM4.

the total cloud fraction will increase the CRE in a linear manner.

The CMIP6 protocol requested the additional diagnostic output consistent with retrievals based on lidar observations from Cloud–Aerosol Lidar and Infrared Pathfinder Satellite Observation (CALIPSO) (Chepfer et al., 2010) and Mod-

erate Resolution Imaging Spectroradiometer (MODIS) imager measurements (Pincus et al., 2012). These are used to evaluate the vertical structure of the clouds in CanAM5 and the ability of CanAM5 to simulate the cloud phase (Fig. 4). Biases in the cross section of cloud amount for CanAM5 relative to the GCM-Oriented CALIPSO Cloud

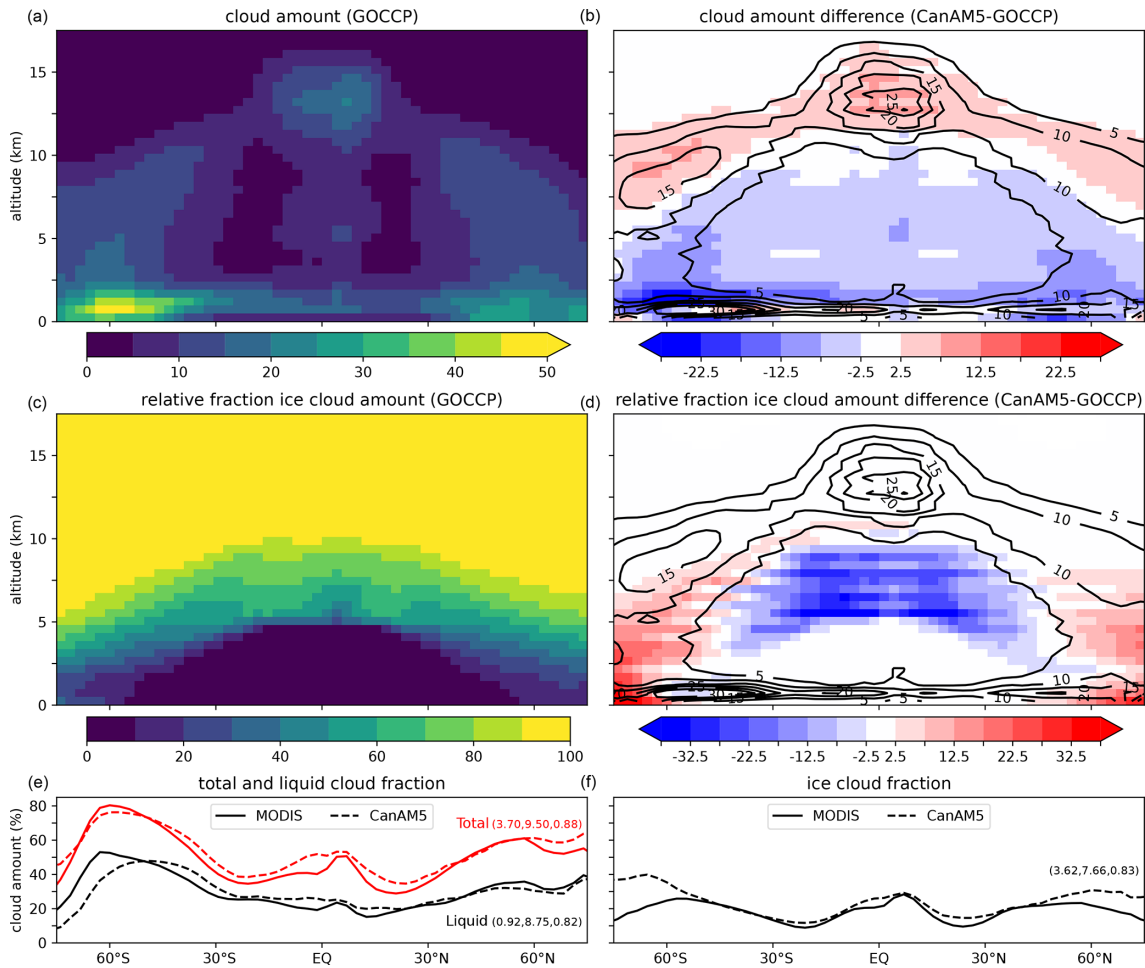


Figure 4. Zonal cloud fraction and cloud phase from CanAM5 compared with GOCCP and MODIS observations averaged over 2007–2009. Black contours in (b) and (d) are the zonal mean cloud fraction from CanAM5. Bracketed numbers in (e) and (f) are, in order, mean bias, root mean square error, and Pearson correlation coefficient, computed using data between 75° S and 75° N.

Product (GOCCP) (upper row Fig. 4) are consistent with biases between CanAM4 and GOCCP (von Salzen et al., 2013). There is generally too much cloud simulated at higher altitudes and too little cloud simulated at lower altitudes.

The middle and lower rows of Fig. 4 use diagnostics of GOCCP cloud-phase profiles and MODIS cloud top phase. In the tropics, CanAM5 underestimates the fraction of cloud that is ice in the middle troposphere; however, it occurs in a range of altitudes where CanAM5 is already simulating too few clouds. The more notable bias is that CanAM5 simulates too much ice cloud poleward of $\sim 50^\circ$, seen in the GOCCP and MODIS diagnostics. These biases in the high-latitude cloud phase can have important consequences on the radiation budget and cloud feedbacks in these regions (Storelvmo et al., 2015).

Precipitation biases are an important feature of any climate model. Although the structure of the biases in CanAM5 is similar to that in CanAM4, there are improvements in some key regions. The most noticeable improvement is the

increased precipitation rate over the Amazon in CanAM5 for most seasons, although dry biases remain (Fig. 5). This change in precipitation is consistent with a reduction in temperatures that are too warm over the Amazon in CanAM5 (Fig. 11), which may be due to more moist conditions suppressing the near-surface temperature.

6.2 Radiation

Radiative fluxes through the top of atmosphere (TOA) and bottom of atmosphere are evaluated using CERES observations (Kato et al., 2018; Loeb et al., 2018). Figure 6 summarizes the global mean climatology for the solar and thermal flux components of the radiative energy budget for CanAM5 and CanAM4. Although a relatively short common period is used from the models and CERES observations (2003–2009), the results are very similar to those using longer periods from CERES (2003–2020) and CanAM (1979–2009).

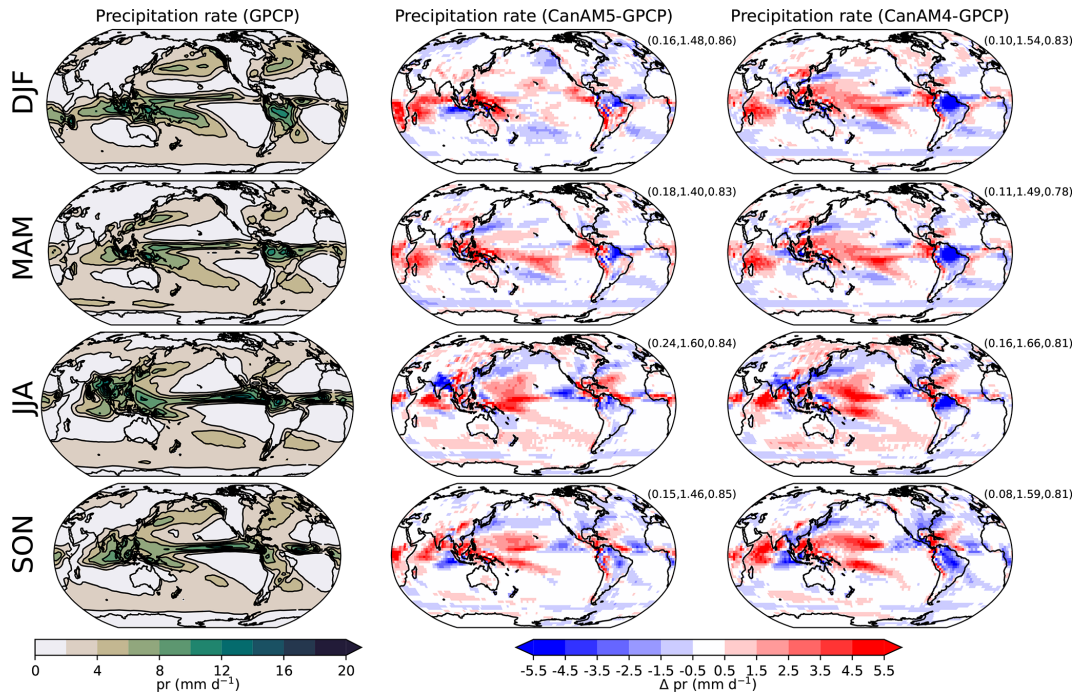


Figure 5. Seasonal mean precipitation rate from GPCP (left column), the bias of CanAM5 relative to GPCP (middle column), and the bias of CanAM4 relative to GPCP (right column). Bracketed numbers to the upper right of difference plots are, in order, mean bias, root mean square error, and Pearson correlation coefficient. All plots use data from the years 1980–2009.

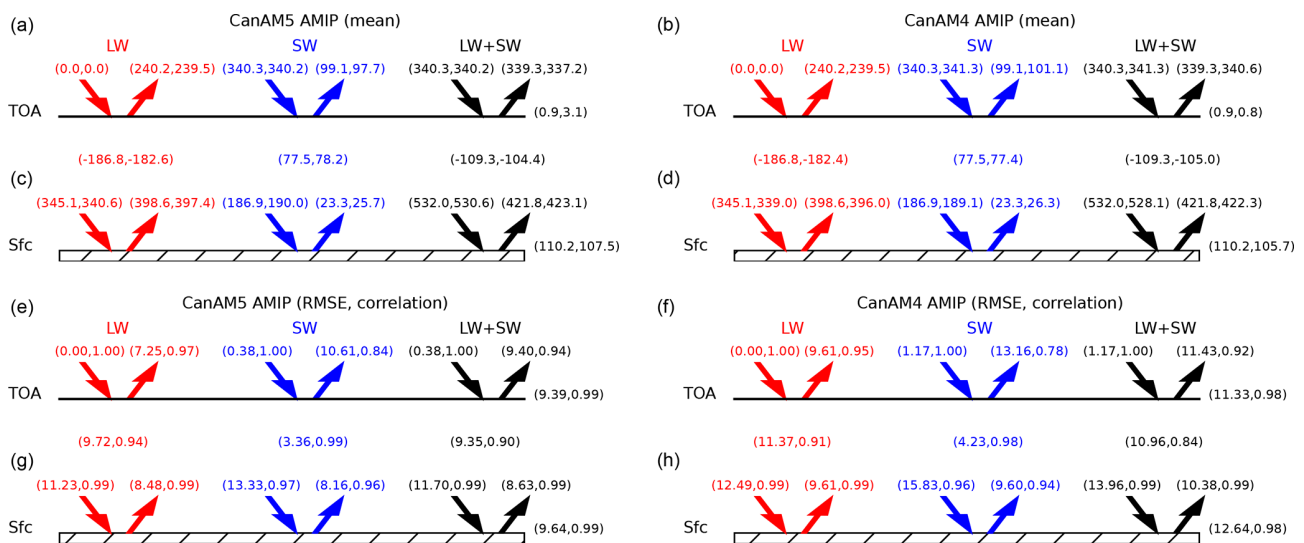


Figure 6. Global and time mean radiative fluxes (shortwave, SW, and longwave, LW) at the top of atmosphere (TOA) and surface, as well as the net flux divergence for the atmosphere, from AMIP simulations by CanAM5 and CanAM4 compared with CERES EBAF. Statistics are computed over the period 2003–2009. For each pair of bracketed numbers in (a)–(d), the left value is CERES and the right value is CanAM. In (e)–(h), the bracketed numbers are root mean square error and Pearson correlation coefficient of CanAM relative to CERES.

We focus first on fluxes at TOA, which can be most directly compared with space-based observations from CERES. The global mean thermal fluxes are effectively identical in CanAM4 and CanAM5. The change in the downward solar flux is due to the use of updated solar forcing (Matthes

et al., 2017) that has a reduced total solar irradiance, which is more consistent with observations and CERES. The upward solar flux is reduced by 3.4 W m^{-2} . There is a small reduction in the clear-sky upward solar flux at TOA, $\sim 0.2 \text{ W m}^{-2}$, so the remainder of this reduction is due to clouds (Fig. 7).

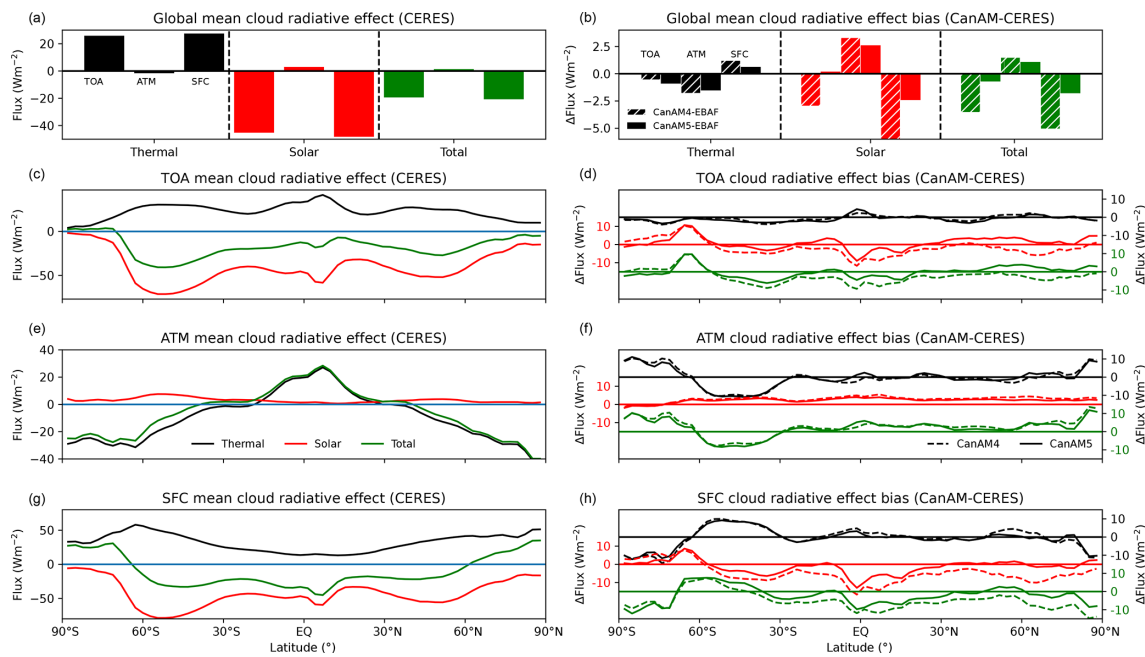


Figure 7. Annual global and zonal mean cloud radiative effects at the top of atmosphere (TOA), atmosphere (ATM), and surface (SFC) from CERES EBAF observations (**a, c, e, g**) and from CanAM5 and CanAM4 AMIP simulations (**b, d, f, h**). The means are averages over 2003–2009.

Evaluated separately, the solar and thermal radiative fluxes are within the range of values from the CMIP6 simulations (Wild, 2020). When all fluxes are combined to compute the net flux imbalance at TOA, CanAM5 has a value that is larger than CERES and CanAM4 by 2.2 W m^{-2} . In CanAM4 there is a compensation between the upward thermal (too small) and upward solar (too large) fluxes, resulting in a net imbalance that is in line with observations, while in CanAM5 both the upward thermal and solar fluxes are smaller than observations. We note that at least one other CMIP6 model documented a similar difference between AMIP and coupled simulations (Hourdin et al., 2021). To put the CanAM5 results into context with other models participating in CMIP6, we compared the net flux at TOA averaged over 2003–2009 for 34 models which had at least one AMIP and one historical coupled simulation. Of the 34 models, 18 AMIP simulations have absolute global mean differences relative to CERES that are greater than 1 W m^{-2} but only three historical coupled simulations have a difference greater than 1 W m^{-2} (not shown). This indicates that the behaviour seen in CanAM5 and CanESM5 is not unique among CMIP6 models.

The TOA flux imbalance is larger than that for coupled CanESM5 simulations, $\sim 1.1 \text{ W m}^{-2}$, averaged over 2003–2009 (Fig. S6). This is mainly due to solar fluxes which are larger (99.3 W m^{-2}) than when using observed SSTs (97.7 W m^{-2}), since upward thermal fluxes at TOA are similar (239.8 W m^{-2} versus 239.5 W m^{-2}). An in-depth analysis of why this occurs is beyond the scope of this paper. Preliminary analysis using CanAM5 with combinations of sea

ice and SST specification, from observations and coupled CanESM5 simulations, suggests that differences in SSTs (Swart et al., 2019) are the main factor which may be due to local and nonlocal responses affecting the TOA radiative fluxes.

While the TOA radiative fluxes were regularly evaluated during the development of CanAM, radiative fluxes at the surface and within the atmosphere were not. For both CanAM5 and CanAM4 the biases at the surface relative to CERES are consistent: downward and upward longwave fluxes that are too small and downward and upward shortwave fluxes that are too large. Altogether this results in too little absorption of radiation at the surface by 3 to 5 W m^{-2} and fairly consistent overestimation of net absorption in the atmosphere by 5 W m^{-2} due mainly to too much absorption of longwave radiation.

Clouds strongly modulate radiative fluxes, so we next examine the simulated cloud radiative effects (CREs), defined as $\text{CRE} = F_{\text{clear sky}} - F_{\text{all sky}}$, where $F_{\text{clear sky}}$ is the radiative flux in the absence of clouds and $F_{\text{all sky}}$ is the radiative flux with clouds present. The annual mean cloud radiative effects are generally positive for longwave and negative for shortwave at TOA and the surface, while the longwave strongly controls the zonal atmospheric CRE (Fig. 7). The global mean CREs simulated by CanAM5 are less biased relative to CERES than CanAM4, especially for shortwave CRE, while the longwave CRE at TOA is slightly more biased than CanAM4 (Fig. 7). Zonal mean CREs show that the improvements seen in the CanAM5 global means are due to

reduced biases at most latitudes (Fig. 7). In addition to improved global mean biases, the root mean square error is decreased (Fig. S1). These improved CREs suggest improved simulation of cloud properties in CanAM5 (Sect. 6.1).

6.3 Circulation

In this subsection we document the climatological properties of the winds, temperature, and surface pressure in CanAM5 for an AMIP experiment. Seasonal climatologies of latitude–height zonal-mean zonal wind fields and anomalies are presented in Fig. 8. While overall biases are similar relative to CanAM4, CanAM5 displays anomalously positive rather than negative wind biases in the mid- to high-latitude Northern Hemisphere DJF lower stratosphere. This is consistent with weaker planetary wave forcing of the Northern Hemisphere stratosphere in CanAM5. This wintertime positive zonal wind bias is associated with a weakening of the orographic gravity-wave drag due to a change in parameter values between the two model versions (Sect. 4). Similarly, this weakening of the gravity wave drag contributes to a larger positive anomaly of zonal-mean zonal winds in CanAM5 in the Southern Hemisphere wintertime stratosphere. The near-surface zonal wind climatology is consistent with the coupled CanESM5 simulations (Swart et al., 2019), with biases relative to ERA5 generally smaller in CanAM5, with the most significant reductions in midlatitudes in both hemispheres (Fig. A1).

In Fig. 9, seasonal climatologies of latitude–height zonal-mean temperature from ERA5, CanAM5, and CanAM4 are presented. In general, CanAM5 and CanAM4 have similar patterns of temperature bias in all seasons, including a warm tropical tropopause and cool extratropical tropopause. However, there are regional and seasonal differences; for example, temperatures between December and May poleward of 60° N in the stratosphere are not as systematically biased warm in CanAM5 relative to CanAM4. The pattern and magnitude of the temperature biases are similar to those in coupled configurations (Swart et al., 2019).

The seasonal mean sea-level pressure is presented in Fig. 10. Relative to CanAM4, CanAM5 displays larger DJF biases in the Aleutian Low and North Pacific High but lower bias in the whole of the Atlantic Ocean in all seasons.

Seasonal mean biases in near-surface temperature for CanAM5 and CanAM4 are presented in Fig. 11. Persistent cold biases are found over the Tibetan Plateau and North Africa in both models. The Tibetan Plateau bias is negatively correlated with snow cover bias (too much snow cover and temperatures that are too cold), a feature found in other CMIP6 models (Lalande et al., 2021). The source of a snow cover that is too large is complex and is present to differing degrees in CanAM4 and CanAM5. That said, it does seem to be a robust feature of CanAM, given that the land model was significantly changed between CanAM4 and CanAM5, including the parameterization of snow albedo (Sect. 3.1). In

North Africa, cold biases are thought to be due to the change from a globally constant albedo for bare soil to a more realistic distribution based on local soil conditions (Lawrence and Chase, 2007).

Warm biases are apparent over the Brazil basin, although somewhat reduced in CanAM5, consistent with biases related to too little precipitation (Fig. 5). Over central North America in JJA, the warm bias persists in CanAM5 and is more extensive than in CanAM4. This is a common warm bias among CMIP5 models during JJA (Cheruy et al., 2014) for which the cause is thought to be a complex interplay between land–atmosphere coupling, radiation, and clouds that rapidly develop in climate models (Morcrette et al., 2018).

7 Conclusions

CanAM5 is the latest atmospheric model from the Canadian Centre for Climate Modelling and Analysis. In this study, we have presented the main model differences between CanAM5 and its predecessor CanAM4. In particular, these differences are primarily related to radiation, clouds, and aerosols; a major update of the land surface model; and the addition of a parameterization of freshwater lakes. Generally, mean climatologies from CanAM5 for near-present conditions, and using observed SSTs and sea ice, are similar to those from CanAM4, with some notable improvements, including reduced precipitation and temperature biases over the Amazonian basin, reduced cloud fraction biases, and a reduction in solar and thermal CREs. Some biases persist from CanAM4 to CanAM5, e.g., cold biases over the Tibetan Plateau, and new biases are present in CanAM5 when using prescribed SSTs and sea ice, e.g., a bias in net downward flux at TOA. As noted, the bias in the net downward flux at TOA is the result of tuning to have a coupled 1850 control simulation with CanESM5 that is close to target global mean temperature and sea ice area (Swart et al., 2019).

Why it was necessary to tune the net downward flux at TOA higher than observations when using observed SSTs and sea ice remains a question for further research. Additional simulations with CanAM5, using combinations of observed SSTs and sea ice with SSTs and sea ice from coupled CanESM5 simulations, suggest that this is due to the SSTs in CanESM5. This was not the case for CanESM2 and CanAM4, which could be largely tuned for coupling using observed SSTs and sea ice. Further analysis, including the use of Green's functions (Zhou et al., 2017) to link regional differences in SSTs to global mean fluxes at TOA, should help inform future tuning of CanESM and CanAM. Another question considered is why CanESM5 has a significantly larger climate sensitivity than CanESM2 and nearly all CMIP6 models (Zelinka et al., 2020). At present, this is thought to be mostly due to changes in cloud feedbacks (Virgin et al., 2021). This suggests that improved mean climatologies of clouds and radiation in CanAM5 and

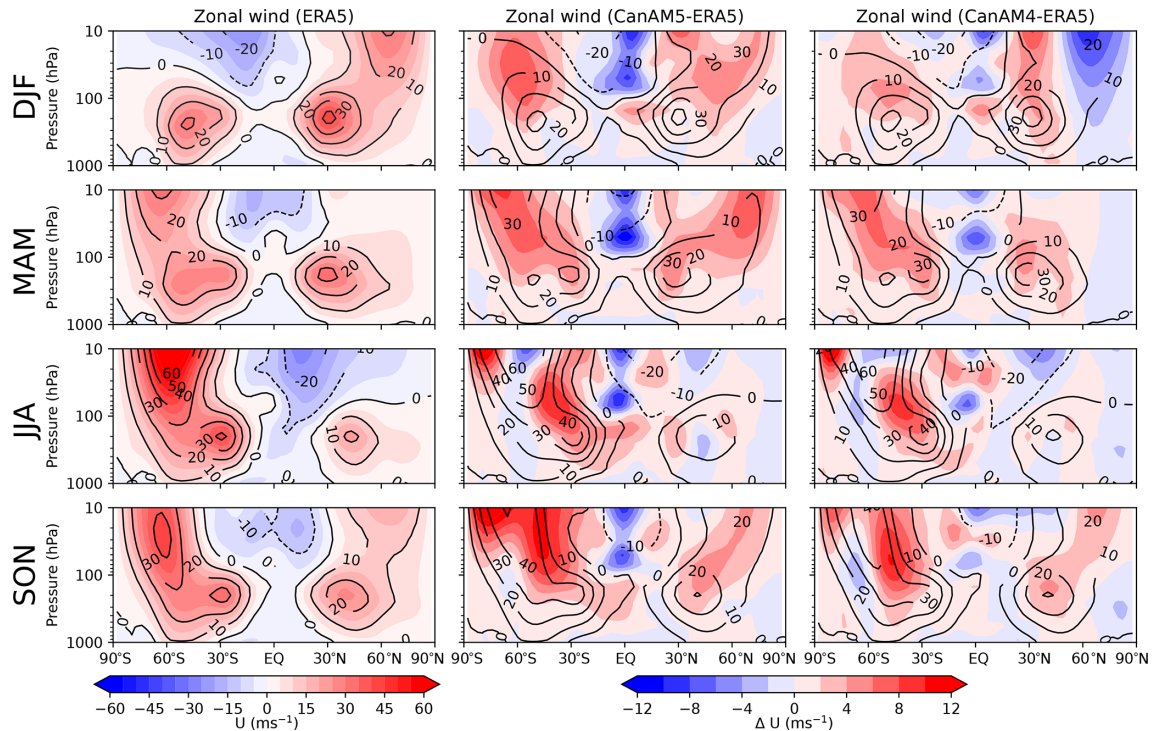


Figure 8. Seasonal mean latitude–pressure plots of zonal wind from ERA5 (left column), the bias of CanAM5 relative to ERA5 (middle column), and the bias of CanAM4 relative to ERA5 (right column). For all plots, contours are the mean. For the ERA5 plot, shading is the mean, and in other plots the shading is the bias relative to ERA5. All plots use data from the years 1980–2009.

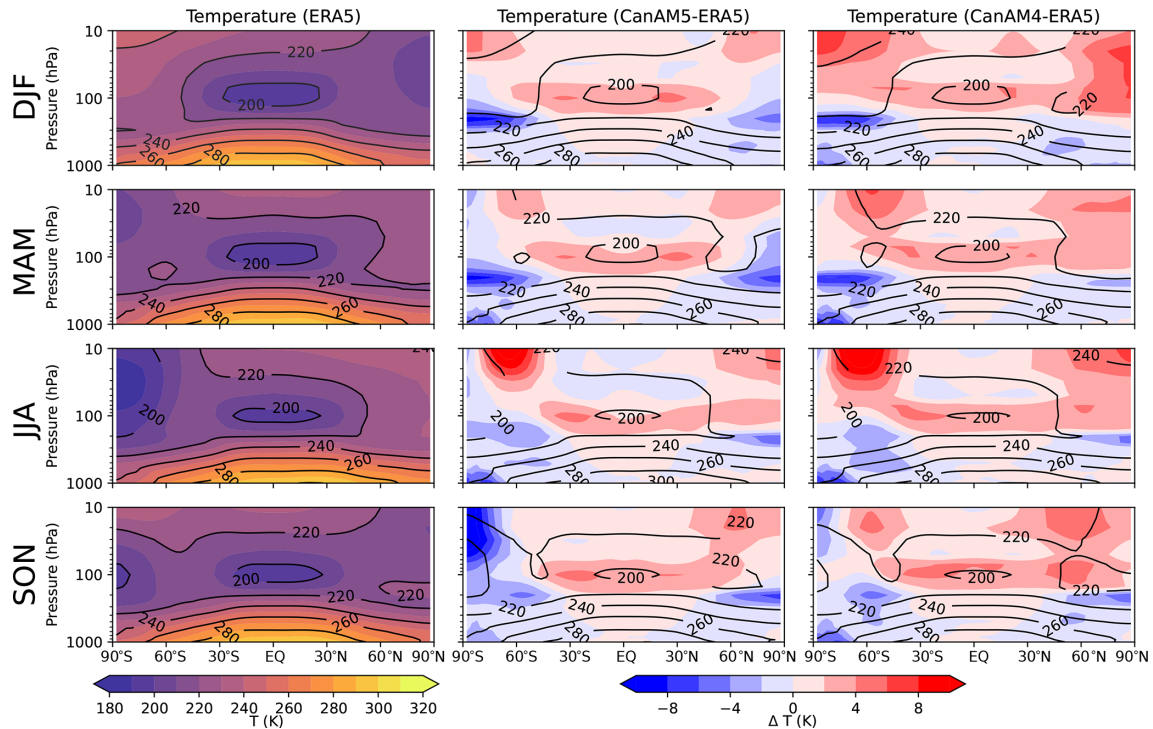


Figure 9. Seasonal mean latitude–pressure plots of temperature from ERA5 (left column), the bias of CanAM5 relative to ERA5 (middle column), and the bias of CanAM4 relative to ERA5 (right column). For all plots, contours are the mean. For the ERA5 plot, shading is the mean, and in other plots the shading is the bias relative to ERA5. All plots use data from the years 1980–2009.

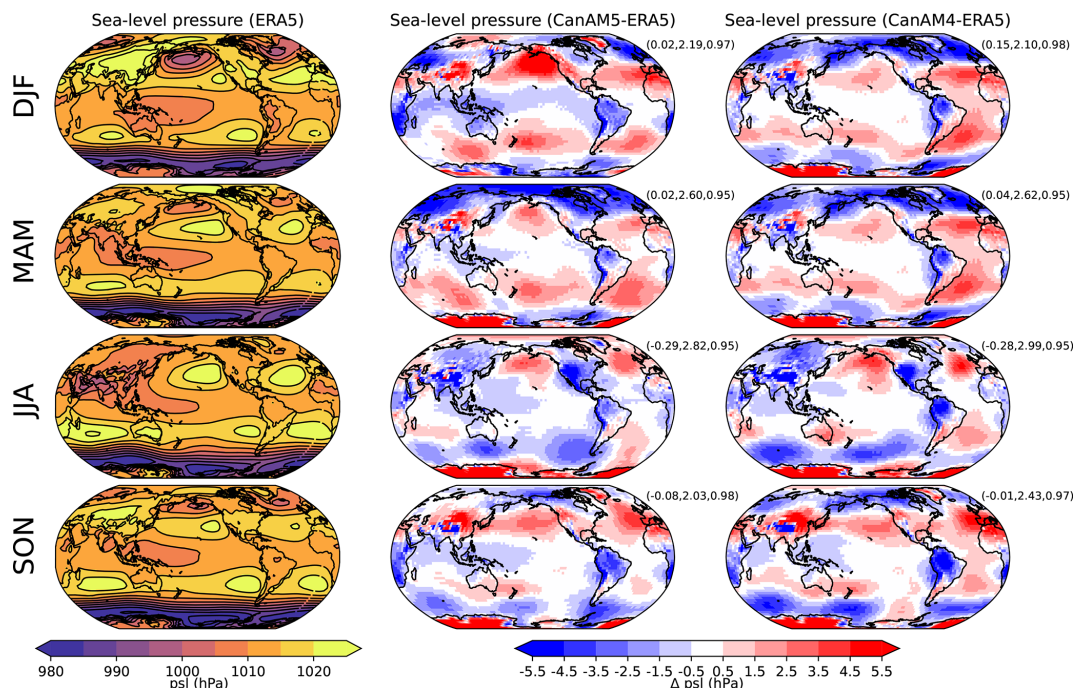


Figure 10. Seasonal mean sea-level pressure from ERA5 (left column), the bias of CanAM5 relative to ERA5 (middle column), and the bias of CanAM4 relative to ERA5 (right column). Bracketed numbers to the upper right of difference plots are, in order, mean bias, root mean square error, and Pearson correlation coefficient. All plots use data from the years 1980–2009.

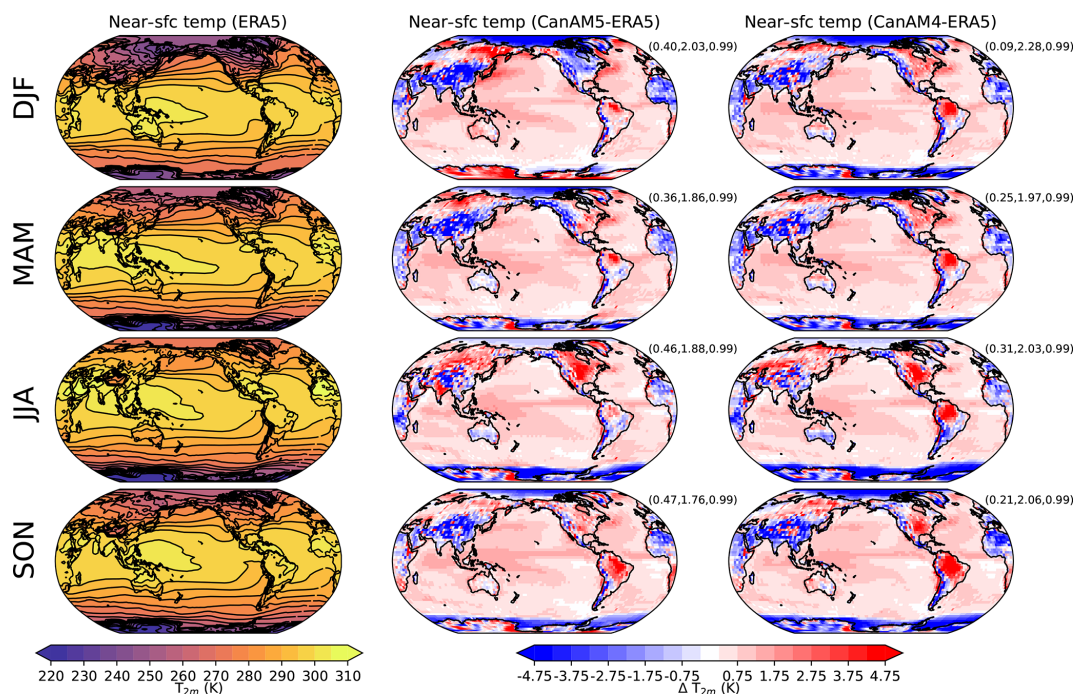


Figure 11. Seasonal mean near-surface temperature from ERA5 (left column), the bias of CanAM5 relative to ERA5 (middle column), and the bias of CanAM4 relative to ERA5 (right column). Bracketed numbers to the upper right of difference plots are, in order, mean bias, root mean square error, and Pearson correlation coefficient. All plots use data from the years 1980–2009.

CanESM5 do not necessarily result in improved cloud feedbacks (Zelinka et al., 2022) and climate sensitivity. A better understanding of both these questions will provide guidance for the ongoing development of CanAM.

Appendix A

Table A1. Observational data used for model evaluation.

Data	Description	Version	Reference
TOA radiative fluxes	CERES EBAF-TOA	4.1	Loeb et al. (2018), NASA/LARC/S-D/ASDC (2019a)
Surface radiative fluxes	CERES EBAF	4.1	Kato et al. (2018), NASA/LARC/S-D/ASDC (2019b)
Lidar-based cloud amount	GOCCP (3D_CloudFraction)	3.1.2	Chepfer et al. (2010)
Lidar-based cloud phase	GOCCP (3D_CloudFraction_phase)	3.1.2	Cesana and Chepfer (2013), Guzman et al. (2023)
Cloud amount histogram	ISCCP H (HGG)	v01r00	Knapp et al. (2021), Guzman et al. (2023), Rossow et al. (2016), NASA/LARC/SD/ASDC (1999)
Cloud amount histogram	ISCCP D	2	Rossow and Schiffer (1999), NASA/LARC/SD/ASDC (1999)
Cloud top phase	MODIS	6	Pincus et al. (2012) http://dx.doi.org/10.5067/MODIS/MCD06COSP_D3_MODIS.061
Atmospheric and surface data	ERA	5	Hersbach et al. (2020) Hersbach et al. (2019a, b)

Table A2. CMIP6 and CMIP5 data used for model evaluation.

Figure number	CMIP6/CMIP5 variable	Description
Figure 2	clisccp	Histogram of cloud amount by cloud top pressure and cloud visible optical thickness
Figure 3	clisccp	Histogram of cloud amount by cloud top pressure and cloud visible optical thickness, consistent with ISCCP
Figure 4	clcalipso, clcalipsoliq, clcalipsoice, clwmodis, climodis, cltmodis	Cloud profile consistent with CALIPSO and cloud fraction from MODIS
Figure 5	pr	Precipitation rate
Figure 6	rsdt, rsut, rlut, rsds, rsus, rlds, rlus	Radiative fluxes at top of atmosphere and surface
Figure 7	rsdt, rsut, rsutcs, rlut, rlutcs, rsds, rsus, rsdscs, rsuscs, rlds, rlus, rldscs	Radiative fluxes at top of atmosphere and surface
Figure 8	ua	Zonal wind
Figure 9	ta	Temperature
Figure 10	psl	Sea-level pressure
Figure 11	tas	Near-surface temperature

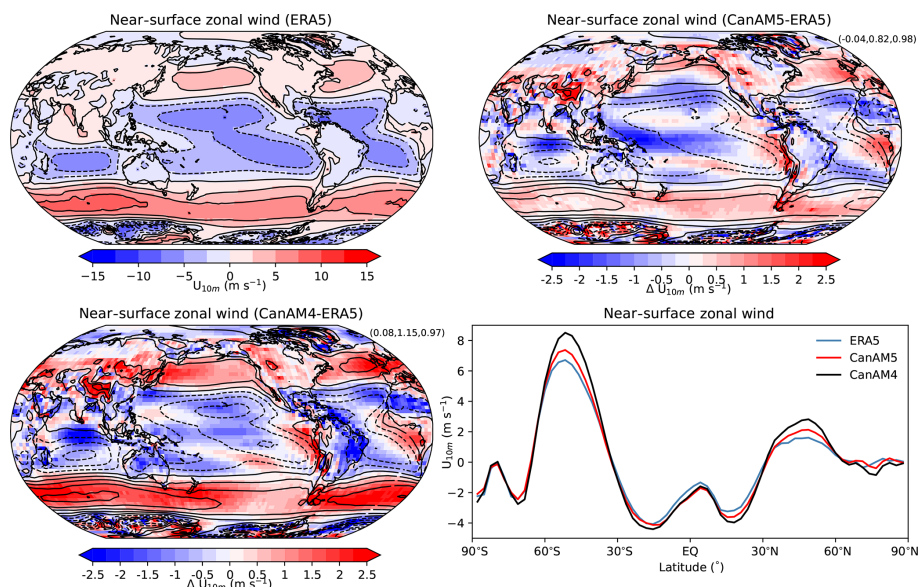


Figure A1. Annual mean near-surface zonal wind, nominally 10 m above the surface from ERA5 (upper left) and CanAM5 and CanAM4 biases. For all plots, contours are the mean. While for the ERA5 plot shading is also the mean, in the other plots the shading is the bias relative to ERA5. Bracketed numbers to the upper right of difference plots are, in order, root mean square error and Pearson correlation coefficient. All plots use data from the years 1980–2009.

Table A3. Acronyms, initialisms, and abbreviations used in the paper.

AMIP	Atmospheric Model Intercomparison Project
CCCma	Canadian Centre for Climate Modelling and Analysis
CanAM	Canadian Atmospheric Model
CanESM	Canadian Earth System Model
CMAM	Canadian Middle Atmosphere Model
CERES	Clouds and the Earth’s Radiant Energy System
CMIP	Coupled Model Intercomparison Project
CFMIP	Cloud Feedback Model Intercomparison Project
CLASS	Canadian Land Surface Scheme
CSLM	Canadian Small Lake Model
CRE	Cloud radiative effect
CALIPSO	Cloud–Aerosol Lidar and Infrared Pathfinder Satellite Observation
DECK	Diagnostic, Evaluation and Characterization of Klima
DJF	December–January–February
ERA	ECMWF (European Centre for Medium-Range Weather Forecasts) Reanalysis
GMMIP	Global Monsoons Model Intercomparison Project
GLD	Global Lake Database
GOCCP	GCM-Oriented Cloud–Aerosol Lidar and Infrared Pathfinder Satellite Observation (CALIPSO) Cloud Product
HITRAN	High-resolution transmission
ISCCP	International Satellite Cloud Climatology Project
JJA	June–July–August
MAM	March–April–May
MODIS	Moderate Resolution Imaging Spectroradiometer
RFMIP	Radiative Forcing Model Intercomparison Project
SON	September–October–November
TOA	Top of atmosphere

Code and data availability. The full CanESM5 source code is publicly available at <https://gitlab.com/ccma/canesm> (last access: 14 September 2023) and includes CanAM5 as a sub-module. The version of the code which can be used to produce all simulations submitted to CMIP6 and described in this paper is tagged as v5.0.3 and has the following associated DOI: <https://doi.org/10.5281/zenodo.3251114> (Swart et al., 2023). The scripts used to produce all the figures are available at <https://doi.org/10.5281/zenodo.7579680> (Cole, 2023). All CanESM5–CanAM5 and CanESM2–CanAM4 simulations conducted for CMIP6 and CMIP5, respectively, including those described in this paper, are publicly available via the Earth System Grid Federation (ESGF). All observational data used are publicly available and are listed in Table A1.

Supplement. The supplement related to this article is available online at: <https://doi.org/10.5194/gmd-16-5427-2023-supplement>.

Author contributions. JNSC drafted the manuscript and created the figures, contributed to development of CanAM5, and performed simulations with CanAM4 and CanAM5 used in the paper. KvS led the development of CanAM5 and wrote the “Aerosols and chemistry” section. JL developed the radiative transfer code and wrote the Radiation section. JS wrote the Tiling, Circulation, and “Clouds and precipitation” sections and contributed to CanAM5 development. DP contributed to CanAM5 development. VA developed CLASS-CTEM and wrote the section that describes it. NM and ML contributed to CanAM5 development. MM developed the Canadian Small Lake Model and wrote the section describing it. DV developed CLASS. All authors contributed to writing the manuscript.

Competing interests. The contact author has declared that none of the authors has any competing interests.

Disclaimer. Publisher’s note: Copernicus Publications remains neutral with regard to jurisdictional claims in published maps and institutional affiliations.

Acknowledgements. We thank Carsten Abraham, Barbara Winter, and two anonymous reviewers for many helpful comments that improved the manuscript. We also thank Barbara Winter for preparing forcing datasets used by CanAM5 for CMIP6 experiments shown in this paper.

Review statement. This paper was edited by Xiaohong Liu and reviewed by two anonymous referees.

References

- Anderson, E. A.: A point energy and mass balance model of a snow cover, Tech. rep., United States National Weather Service, <https://repository.library.noaa.gov/view/noaa/6392>, 1976.
- Arora, V. K. and Boer, G. J.: A parameterization of leaf phenology for the terrestrial ecosystem component of climate models, *Global Change Biol.*, 11, 39–59, <https://doi.org/10.1111/j.1365-2486.2004.00890.x>, 2005.
- Arora, V. K., Scinocca, J. F., Boer, G. J., Christian, J. R., Denman, K. L., Flato, G. M., Kharin, V. V., Lee, W. G., and Merryfield, W. J.: Carbon emission limits required to satisfy future representative concentration pathways of greenhouse gases, *Geophys. Res. Lett.*, 38, L05805, <https://doi.org/10.1029/2010GL046270>, 2011.
- Arora, V. K., Melton, J. R., and Plummer, D.: An assessment of natural methane fluxes simulated by the CLASS-CTEM model, *Biogeosciences*, 15, 4683–4709, <https://doi.org/10.5194/bg-15-4683-2018>, 2018.
- Bartlett, P. A. and Verseghy, D. L.: Modified treatment of intercepted snow improves the simulated forest albedo in the Canadian Land Surface Scheme, *Hydrol. Process.*, 29, 3208–3226, <https://doi.org/10.1002/hyp.10431>, 2015.
- Bartlett, P. A., MacKay, M. D., and Verseghy, D. L.: Modified snow algorithms in the Canadian land surface scheme: Model runs and sensitivity analysis at three boreal forest stands, *Atmosphere-Ocean*, 44, 207–222, <https://doi.org/10.3137/ao.440301>, 2006.
- Baum, B. A., Yang, P., Heymsfield, A. J., Schmitt, C. G., Xie, Y., Bansemer, A., Hu, Y.-X., and Zhang, Z.: Improvements in Shortwave Bulk Scattering and Absorption Models for the Remote Sensing of Ice Clouds, *J. Appl. Meteorol. Climatol.*, 50, 1037–1056, <https://doi.org/10.1175/2010JAMC2608.1>, 2011.
- Bodas-Salcedo, A., Webb, M. J., Bony, S., Chepfer, H., Dufresne, J.-L., Klein, S. A., Zhang, Y., Marchand, R., Haynes, J. M., Pincus, R., and John, V. O.: COSP: Satellite simulation software for model assessment, *B. Am. Meteorol. Soc.*, 92, 1023–1043, <https://doi.org/10.1175/2011BAMS2856.1>, 2011.
- Cesana, G. and Chepfer, H.: Evaluation of the cloud thermodynamic phase in a climate model using CALIPSO-GOCCP, *J. Geophys. Res.-Atmos.*, 118, 7922–7937, <https://doi.org/10.1002/jgrd.50376>, 2013.
- Chen, X., Huang, X., and Flanner, M. G.: Sensitivity of modeled far-IR radiation budgets in polar continents to treatments of snow surface and ice cloud radiative properties, *Geophys. Res. Lett.*, 41, 6530–6537, <https://doi.org/10.1002/2014GL061216>, 2014.
- Chepfer, H., Bony, S., Winker, D., Cesana, G., Dufresne, J. L., Minnis, P., Stubenrauch, C. J., and Zeng, S.: The GCM-Oriented CALIPSO Cloud Product (CALIPSO-GOCCP), *J. Geophys. Res.*, 115, D00H16, <https://doi.org/10.1029/2009JD012251>, 2010.
- Cheruy, F., Dufresne, J. L., Hourdin, F., and Ducharne, A.: Role of clouds and land-atmosphere coupling in midlatitude continental summer warm biases and climate change amplification in CMIP5 simulations, *Geophys. Res. Lett.*, 41, 6493–6500, <https://doi.org/10.1002/2014GL061145>, 2014.
- Choulga, M., Kourzeneva, E., Zakharova, E., and Doganovsky, A.: Estimation of the mean depth of boreal lakes for use in numerical weather prediction and climate modelling, *Tellus A*, 66, 21295, <https://doi.org/10.3402/tellusa.v66.21295>, 2014.

- Cole, J.: Figures for CanAM5 paper – v1.0.0 (v1.0.0), Zenodo [code], <https://doi.org/10.5281/zenodo.7579680>, 2023.
- Comer, N. T., Lafleur, P. M., Roulet, N. T., Letts, M. G., Skarupa, M., and Verseghy, D.: A test of the Canadian land surface scheme (class) for a variety of wetland types, *Atmosphere-Ocean*, 38, 161–179, <https://doi.org/10.1080/07055900.2000.9649644>, 2000.
- Côté, J. and Konrad, J.-M.: A generalized thermal conductivity model for soils and construction materials, *Can. Geotech. J.*, 42, 443–458, <https://doi.org/10.1139/t04-106>, 2005.
- Dingman, S., L.: Physical hydrology, Prentice-Hall, Upper Saddle River, NJ, USA, 2nd edn., ISBN 9780130996954, 2002.
- Ebert, E. E. and Curry, J. A.: An intermediate one-dimensional thermodynamic sea ice model for investigating ice-atmosphere interactions, *J. Geophys. Res.-Oceans*, 98, 10085–10109, <https://doi.org/10.1029/93JC00656>, 1993.
- ECMWF: IFS Documentation CY25R1 – Part IV: Physical Processes, in: IFS Documentation CY25R1, edited by: White, P., no. 4 in IFS Documentation, ECMWF, <https://doi.org/10.21957/6hswlclmt>, 2003.
- Eyring, V., Bony, S., Meehl, G. A., Senior, C. A., Stevens, B., Stouffer, R. J., and Taylor, K. E.: Overview of the Coupled Model Intercomparison Project Phase 6 (CMIP6) experimental design and organization, *Geosci. Model Dev.*, 9, 1937–1958, <https://doi.org/10.5194/gmd-9-1937-2016>, 2016.
- Farmer, D. M. and Carmack, E.: Wind Mixing and Restratification in a Lake near the Temperature of Maximum Density, *J. Phys. Oceanogr.*, 11, 1516–1533, [https://doi.org/10.1175/1520-0485\(1981\)011<1516:WMARIA>2.0.CO;2](https://doi.org/10.1175/1520-0485(1981)011<1516:WMARIA>2.0.CO;2), 1981.
- Fichefet, T. and Maqueda, M. A. M.: Sensitivity of a global sea ice model to the treatment of ice thermodynamics and dynamics, *J. Geophys. Res.-Oceans*, 102, 12609–12646, <https://doi.org/10.1029/97JC00480>, 1997.
- Flanner, M. G., Liu, X., Zhou, C., Penner, J. E., and Jiao, C.: Enhanced solar energy absorption by internally-mixed black carbon in snow grains, *Atmos. Chem. Phys.*, 12, 4699–4721, <https://doi.org/10.5194/acp-12-4699-2012>, 2012.
- Frouin, R., Iacobellis, S. F., and Deschamps, P.-Y.: Influence of oceanic whitecaps on the Global Radiation Budget, *Geophys. Res. Lett.*, 28, 1523–1526, <https://doi.org/10.1029/2000GL012657>, 2001.
- Garratt, J. R.: The atmospheric boundary layer, Cambridge University Press Cambridge, New York, New York, USA, ISBN 0-521-38052-9, 1992.
- Gottelman, A., Morrison, H., Santos, S., Bogenschutz, P., and Caldwell, P. M.: Advanced Two-Moment Bulk Microphysics for Global Models. Part II: Global Model Solutions and Aerosol-Cloud Interactions, *J. Climate*, 28, 1288–1307, <https://doi.org/10.1175/JCLI-D-14-00103.1> 2015.
- Ghan, S. J., Smith, S. J., Wang, M., Zhang, K., Pringle, K., Carslaw, K., Pierce, J., Bauer, S., and Adams, P.: A simple model of global aerosol indirect effects, *J. Geophys. Res.-Atmos.*, 118, 6688–6707, <https://doi.org/10.1002/jgrd.50567>, 2013.
- Guzman, R., Chepfer, H., and Bony, S.: GCM-Oriented CALIPSO Cloud Product, Climserv [data set], https://climserv.ipsl.polytechnique.fr/cfmip-obs/Calipso_goccp.html, last access: 15 February 2023.
- Hedstrom, N. R. and Pomeroy, J. W.: Measurements and modelling of snow interception in the boreal forest, *Hydrol. Process.*, 12, 1611–1625, [https://doi.org/10.1002/\(SICI\)1099-1085\(199808/09\)12:10/11<1611::AID-HYP684>3.0.CO;2-4](https://doi.org/10.1002/(SICI)1099-1085(199808/09)12:10/11<1611::AID-HYP684>3.0.CO;2-4), 1998.
- Hersbach, H., Bell, B., Berriford, P., Berrisford, G., Horányi, A., Muñoz-Sabater, J., Nicolas, J., Peubey, C., Radu, R., Rozum, I., Schepers, D., Simmons, A., Soci, C., Dee, D., and Thépaut, J.-N.: ERA5 monthly data on pressure levels from 1959 to present, Copernicus Climate Change Service (C3S) Climate Data Store (CDS), <https://doi.org/10.24381/cds.6860a573>, 2019a.
- Hersbach, H., Bell, B., Berriford, P., Berrisford, G., Horányi, A., Muñoz-Sabater, J., Nicolas, J., Peubey, C., Radu, R., Rozum, I., Schepers, D., Simmons, A., Soci, C., Dee, D., and Thépaut, J.-N.: ERA5 monthly data on single levels from 1959 to present, Copernicus Climate Change Service (C3S) Climate Data Store (CDS), <https://doi.org/10.24381/cds.f17050d7>, 2019b.
- Hersbach, H., Bell, B., Berrisford, P., Hirahara, S., Horányi, A., Muñoz-Sabater, J., Nicolas, J., Peubey, C., Radu, R., Schepers, D., Simmons, A., Soci, C., Abdalla, S., Abellan, X., Balsamo, G., Bechtold, P., Biavati, G., Bidlot, J., Bonavita, M., De Chiara, G., Dahlgren, P., Dee, D., Diamantakis, M., Dragani, R., Flemming, J., Forbes, R., Fuentes, M., Geer, A., Haimberger, L., Healy, S., Hogan, R. J., Hólm, E., Janisková, M., Keeley, S., Laloyaux, P., Lopez, P., Lupu, C., Radnoti, G., de Rosnay, P., Rozum, I., Vamborg, F., Villaume, S., and Thépaut, J.-N.: The ERA5 global reanalysis, *Q. J. Roy. Meteor. Soc.*, 146, 1999–2049, <https://doi.org/10.1002/qj.3803>, 2020.
- Hourdin, F., Williamson, D., Rio, C., Couvreux, F., Roehrig, R., Villefranque, N., Musat, I., Fairhead, L., Diallo, F. B., and Volodina, V.: Process-Based Climate Model Development Harnessing Machine Learning: II. Model Calibration From Single Column to Global, *J. Adv. Model. Earth Sy.*, 13, e2020MS002225, <https://doi.org/10.1029/2020MS002225>, 2021.
- Imberger, J.: The diurnal mixed layer1, *Limnol. Oceanogr.*, 30, 737–770, <https://doi.org/10.4319/lo.1985.30.4.0737>, 1985.
- Jin, Z., Qiao, Y., Wang, Y., Fang, Y., and Yi, W.: A new parameterization of spectral and broadband ocean surface albedo, *Opt. Express*, 19, 26429–26443, <https://doi.org/10.1364/OE.19.026429>, 2011.
- Kato, S., Rose, F. G., Rutan, D. A., Thorsen, T. J., Loeb, N. G., Doelling, D. R., Huang, X., Smith, W. L., Su, W., and Ham, S.-H.: Surface Irradiances of Edition 4.0 Clouds and the Earth’s Radiant Energy System (CERES) Energy Balanced and Filled (EBAF) Data Product, *J. Climate*, 31, 4501–4527, <https://doi.org/10.1175/JCLI-D-17-0523.1>, 2018.
- Khairoutdinov, M. and Kogan, Y.: A New Cloud Physics Parameterization in a Large-Eddy Simulation Model of Marine Stratocumulus, *Mon. Weather Rev.*, 128, 229–243, [https://doi.org/10.1175/1520-0493\(2000\)128<0229:ANCPPI>2.0.CO;2](https://doi.org/10.1175/1520-0493(2000)128<0229:ANCPPI>2.0.CO;2), 2000.
- Klein, S. A., Zhang, Y., Zelinka, M. D., Pincus, R., Boyle, J., and Gleckler, P. J.: Are climate model simulations of clouds improving? An evaluation using the ISCCP simulator, *J. Geophys. Res.-Atmos.*, 118, 1329–1342, <https://doi.org/10.1002/jgrd.50141>, 2013.
- Knapp, K. R., Young, A. H., Semunegus, H., Inamdar, A. K., and Hankins, W.: Adjusting ISCCP Cloud Detection to Increase Consistency of Cloud Amount and Reduce Artifacts, *J. Atmos. Ocean. Tech.*, 38, 155–165, <https://doi.org/10.1175/JTECH-D-20-0045.1>, 2021.

- Kourzeneva, E., Asensio, H., Martin, E., and Faroux, S.: Global gridded dataset of lake coverage and lake depth for use in numerical weather prediction and climate modelling, *Tellus A*, 64, 15640, <https://doi.org/10.3402/tellusa.v64i0.15640>, 2012.
- Lalande, M., Ménégoz, M., Krinner, G., Naegeli, K., and Wunderle, S.: Climate change in the High Mountain Asia in CMIP6, *Earth Syst. Dynam.*, 12, 1061–1098, <https://doi.org/10.5194/esd-12-1061-2021>, 2021.
- Lawrence, P. J. and Chase, T. N.: Representing a new MODIS consistent land surface in the Community Land Model (CLM 3.0), *J. Geophys. Res.-Biogeo.*, 112, G01023, <https://doi.org/10.1029/2006JG000168>, 2007.
- Lebsock, M., Morrison, H., and Gettelman, A.: Microphysical implications of cloud-precipitation covariance derived from satellite remote sensing, *J. Geophys. Res.-Atmos.*, 118, 6521–6533, <https://doi.org/10.1002/jgrd.50347>, 2013.
- Lee, T. J. and Pielke, R. A.: Estimating the Soil Surface Specific Humidity, *J. Appl. Meteorol. Climatol.*, 31, 480–484, [https://doi.org/10.1175/1520-0450\(1992\)031<0480:ETSSSH>2.0.CO;2](https://doi.org/10.1175/1520-0450(1992)031<0480:ETSSSH>2.0.CO;2), 1992.
- Leppäranta, M. and Wang, K.: The ice cover on small and large lakes: scaling analysis and mathematical modelling, *Hydrobiologia*, 599, 183–189, <https://doi.org/10.1007/s10750-007-9201-3>, 2008.
- Letts, M. G., Roulet, N. T., Comer, N. T., Skarupa, M. R., and Verseghy, D. L.: Parametrization of peatland hydraulic properties for the Canadian land surface scheme, *Atmosphere-Ocean*, 38, 141–160, <https://doi.org/10.1080/07055900.2000.9649643>, 2000.
- Li, J., von Salzen, K., Peng, Y., Zhang, H., and Liang, X.: Evaluation of black carbon semidirect radiative effect in a climate model, *J. Geophys. Res.-Atmos.*, 118, 4715–4728, <https://doi.org/10.1002/jgrd.50327>, 2013.
- Liu, Y. and Daum, P. H.: Parameterization of the Autoconversion Process. Part I: Analytical Formulation of the Kessler-Type Parameterizations, *J. Atmos. Sci.*, 61, 1539–1548, [https://doi.org/10.1175/1520-0469\(2004\)061<1539:POTAPI>2.0.CO;2](https://doi.org/10.1175/1520-0469(2004)061<1539:POTAPI>2.0.CO;2), 2004.
- Loeb, N. G., Doelling, D. R., Wang, H., Su, W., Nguyen, C., Corbett, J. G., Liang, L., Mitrescu, C., Rose, F. G., and Kato, S.: Clouds and the Earth's Radiant Energy System (CERES) Energy Balanced and Filled (EBAF) Top-of-Atmosphere (TOA) Edition-4.0 Data Product, *J. Climate*, 31, 895–918, <https://doi.org/10.1175/JCLI-D-17-0208.1>, 2018.
- Ma, X., von Salzen, K., and Li, J.: Modelling sea salt aerosol and its direct and indirect effects on climate, *Atmos. Chem. Phys.*, 8, 1311–1327, <https://doi.org/10.5194/acp-8-1311-2008>, 2008.
- MacKay, M. D.: A Process-Oriented Small Lake Scheme for Coupled Climate Modeling Applications, *J. Hydrometeorol.*, 13, 1911–1924, <https://doi.org/10.1175/JHM-D-11-0116.1>, 2012.
- MacKay, M. D., Verseghy, D. L., Fortin, V., and Rennie, M. D.: Wintertime Simulations of a Boreal Lake with the Canadian Small Lake Model, *J. Hydrometeorol.*, 18, 2143–2160, <https://doi.org/10.1175/JHM-D-16-0268.1>, 2017.
- Matthes, K., Funke, B., Andersson, M. E., Barnard, L., Beer, J., Charbonneau, P., Clilverd, M. A., Dudok de Wit, T., Haber-reiter, M., Hendry, A., Jackman, C. H., Kretzschmar, M., Kruschke, T., Kunze, M., Langematz, U., Marsh, D. R., Maycock, A. C., Misios, S., Rodger, C. J., Scaife, A. A., Seppälä, A., Shangguan, M., Sinnhuber, M., Tourpali, K., Usoskin, I., van de Kamp, M., Verronen, P. T., and Versick, S.: Solar forcing for CMIP6 (v3.2), *Geosci. Model Dev.*, 10, 2247–2302, <https://doi.org/10.5194/gmd-10-2247-2017>, 2017.
- McLandress, C., Scinocca, J. F., Shepherd, T. G., Reader, M. C., and Manney, G. L.: Dynamical Control of the Mesosphere by Orographic and Nonorographic Gravity Wave Drag during the Extended Northern Winters of 2006 and 2009, *J. Atmos. Sci.*, 70, 2152–2169, <https://doi.org/10.1175/JAS-D-12-0297.1>, 2013.
- Michibata, T., Suzuki, K., Sekiguchi, M., and Takemura, T.: Prognostic Precipitation in the MIROC6-SPRINTARS GCM: Description and Evaluation Against Satellite Observations, *J. Adv. Model. Earth Sy.*, 11, 839–860, <https://doi.org/10.1029/2018MS001596>, 2019.
- Mlawer, E. J., Taubman, S. J., Brown, P. D., and Iacono, M. J.: Radiative transfer for inhomogeneous atmospheres: RRTM, a validated correlated-k model for the longwave, *J. Geophys. Res.*, 102, 16663–16682, 1997.
- Morcrette, C. J., Van Weverberg, K., Ma, H.-Y., Ahlgrimm, M., Bazile, E., Berg, L. K., Cheng, A., Cheruy, F., Cole, J., Forbes, R., Gustafson Jr, W. I., Huang, M., Lee, W.-S., Liu, Y., Mellul, L., Merryfield, W. J., Qian, Y., Roehrig, R., Wang, Y.-C., Xie, S., Xu, K.-M., Zhang, C., Klein, S., and Petch, J.: Introduction to CAUSES: Description of Weather and Climate Models and Their Near-Surface Temperature Errors in 5 day Hindcasts Near the Southern Great Plains, *J. Geophys. Res.-Atmos.*, 123, 2655–2683, <https://doi.org/10.1002/2017JD027199>, 2018.
- Namazi, M., von Salzen, K., and Cole, J. N. S.: Simulation of black carbon in snow and its climate impact in the Canadian Global Climate Model, *Atmos. Chem. Phys.*, 15, 10887–10904, <https://doi.org/10.5194/acp-15-10887-2015>, 2015.
- NASA/LARC/SD/ASDC: International Satellite Cloud Climatology Project (ISCCP) Stage D2 Monthly Cloud Products - Revised Algorithm in Hierarchical Data Format, NASA Langley Atmospheric Science Data Center DAAC [data set], <https://doi.org/10.5067/ISCCP/D2>, 1999.
- NASA/LARC/SD/ASDC: CERES Energy Balanced and Filled (EBAF) TOA Monthly means data in netCDF Edition 4.1, NASA Langley Atmospheric Science Data Center DAAC [data set], https://doi.org/10.5067/TERRA-AQUA/CERES/EBAF-TOA_L3B004.1, 2019a.
- NASA/LARC/SD/ASDC: CERES Energy Balanced and Filled (EBAF) TOA and Surface Monthly means data in netCDF Edition 4.1, NASA Langley Atmospheric Science Data Center DAAC [data set], https://doi.org/10.5067/TERRA-AQUA/CERES/EBAF_L3B.004.1, 2019b.
- Niiler, P. and Kraus, E. B.: One-dimensional models of the upper ocean, in: *Modelling and prediction of the upper layers of the ocean*, edited by: Kraus, E., 143–172, Pergamon Press, 1977.
- Oleson, W. B., Lawrence, M., Bonan, B., Flanner, G., Kluzek, E., Lawrence, J., Levis, S., Swenson, C. L., Thornton, E., Dai, A., Decker, M., Dickinson, R. E., Feddes, J. J., Heald, G., Hoffman, F. M., Lamarque, J.-F., Mahowald, N. M., Niu, G., Qian, T., Randerson, J. T., Running, S. W., Sakaguchi, K., Slater, A., Stöckli, R., Wang, A., Yang, Z.-L., Zeng, X., and Zeng, X.: Technical Description of version 4.0 of the Community Land Model (CLM), <https://doi.org/10.5065/D6FB50WZ>, 2010.
- Peng, Y., von Salzen, K., and Li, J.: Simulation of mineral dust aerosol with Piecewise Log-normal Approximation

- (PLA) in CanAM4-PAM, *Atmos. Chem. Phys.*, 12, 6891–6914, <https://doi.org/10.5194/acp-12-6891-2012>, 2012.
- Pincus, R., Platnick, S., Ackerman, S. A., Hemler, R. S., and Hofmann, R. J. P.: Reconciling Simulated and Observed Views of Clouds: MODIS, ISCCP, and the Limits of Instrument Simulators, *J. Climate*, 25, 4699–4720, <https://doi.org/10.1175/JCLI-D-11-00267.1>, 2012.
- Pincus, R., Mlawer, E. J., Oreopoulos, L., Ackerman, A. S., Baek, S., Brath, M., Buehler, S. A., Cady-Pereira, K. E., Cole, J. N. S., Dufresne, J.-L., Kelley, M., Li, J., Manners, J., Paynter, D. J., Roehrig, R., Sekiguchi, M., and Schwarzkopf, D. M.: Radiative flux and forcing parameterization error in aerosol-free clear skies, *Geophys. Res. Lett.*, 42, 5485–5492, <https://doi.org/10.1002/2015GL064291>, 2015.
- Pincus, R., Forster, P. M., and Stevens, B.: The Radiative Forcing Model Intercomparison Project (RFMIP): experimental protocol for CMIP6, *Geosci. Model Dev.*, 9, 3447–3460, <https://doi.org/10.5194/gmd-9-3447-2016>, 2016.
- Pomeroy, J. W. and Gray, D. M.: Snowcover : accumulation, relocation, and management, Tech. Rep. 7, National Hydrology Research Institute (Canada), Saskatoon, Saskatchewan, <http://publications.gc.ca/pub?id=9.892773&sl=0> (last access: 14 September 2023), 1995.
- Rayner, K. N.: Diurnal energetics of a reservoir surface layer, *Environ. Dyn. Rep.* ED-80-005, University of Western Australia, 1980.
- Rossow, W. B. and Schiffer, R. A.: Advances in Understanding Clouds from ISCCP, *B. Am. Meteorol. Soc.*, 80, 2261–2288, 1999.
- Rossow, W. B., Walker, A., Golea, V., Knapp, K. R., Young, A., Inamdar, A. K., Hankins, B., and NOAA's Climate Data Record Program: International Satellite Cloud Climatology Project Climate Data Record, H-Series HGG NOAA National Centers for Environmental Information, <https://doi.org/10.7289/V5QZ281S>, 2016.
- Rothman, L. S., Gordon, I. E., Babikov, Y., Barbe, A., Benner, D. C., Bernath, P. F., Birk, M., Bizzocchi, L., Boudon, V., Brown, L. R., Campargue, A., Chance, K., Cohen, E. A., Coudert, L. H., Devi, V. M., Drouin, B. J., Fayt, A., Flaud, J.-M., Gamache, R. R., Harrison, J. J., Hartmann, J.-M., Hill, C., Hodges, J. T., Jacquemart, D., Jolly, A., Lamouroux, J., Roy, R. J. L., Li, G., Long, D. A., Lyulin, O. M., Mackie, C. J., Massie, S. T., Mikhailenko, S., Müller, H. S. P., Naumenko, O. V., Nikitin, A. V., Orphal, J., Perevalov, V., Perrin, A., Polovtseva, E. R., Richard, C., Smith, M. A. H., Starikova, E., Sung, K., Tashkun, S., Tennyson, J., Toon, G. C., Tyuterev, V. G., and Wagner, G.: The HITRAN2012 molecular spectroscopic database, *J. Quant. Spectrosc. Ra.*, 130, 4–50, <https://doi.org/10.1016/j.jqsrt.2013.07.002>, 2013.
- Sant, V., Posselt, R., and Lohmann, U.: Prognostic precipitation with three liquid water classes in the ECHAM5–HAM GCM, *Atmos. Chem. Phys.*, 15, 8717–8738, <https://doi.org/10.5194/acp-15-8717-2015>, 2015.
- Schmidt, R. A. and Gluns, D. R.: Snowfall interception on branches of three conifer species, *Can. J. Forest Res.*, 21, 1262–1269, <https://doi.org/10.1139/x91-176>, 1991.
- Scinocca, J. F. and McFarlane, N. A.: The parametrization of drag induced by stratified flow over anisotropic orography, *Q. J. Roy. Meteor. Soc.*, 126, 2353–2393, <https://doi.org/10.1002/qj.49712656802>, 2000.
- Scinocca, J. F., McFarlane, N. A., Lazare, M., Li, J., and Plummer, D.: Technical Note: The CCCma third generation AGCM and its extension into the middle atmosphere, *Atmos. Chem. Phys.*, 8, 7055–7074, <https://doi.org/10.5194/acp-8-7055-2008>, 2008.
- Smith, C. J., Kramer, R. J., Myhre, G., Alterskjær, K., Collins, W., Sima, A., Boucher, O., Dufresne, J.-L., Nabat, P., Michou, M., Yukimoto, S., Cole, J., Paynter, D., Shiogama, H., O'Connor, F. M., Robertson, E., Wiltshire, A., Andrews, T., Hannay, C., Miller, R., Nazarenko, L., Kirkevåg, A., Olivie, D., Fiedler, S., Lewinschal, A., Mackallah, C., Dix, M., Pincus, R., and Forster, P. M.: Effective radiative forcing and adjustments in CMIP6 models, *Atmos. Chem. Phys.*, 20, 9591–9618, <https://doi.org/10.5194/acp-20-9591-2020>, 2020.
- Soulis, E. D., Craig, J. R., Fortin, V., and Liu, G.: A simple expression for the bulk field capacity of a sloping soil horizon, *Hydrol. Process.*, 25, 112–116, <https://doi.org/10.1002/hyp.7827>, 2011.
- Spigel, R. H., Imberger, J., and Rayner, K. N.: Modeling the diurnal mixed layer, *Limnol. Oceanogr.*, 31, 533–556, <https://doi.org/10.4319/lo.1986.31.3.0533>, 1986.
- Storelvmo, T., Tan, I., and Korolev, A. V.: Cloud Phase Changes Induced by CO₂ Warming – a Powerful yet Poorly Constrained Cloud-Climate Feedback, *Current Climate Change Reports*, 1, 288–296, <https://doi.org/10.1007/s40641-015-0026-2>, 2015.
- Stubenrauch, C. J., Rossow, W. B., Kinne, S., Ackerman, S., Cesana, G., Chepfer, H., Di Girolamo, L., Getzewich, B., Guignard, A., Heidinger, A., Maddux, B. C., Menzel, W. P., Minnis, P., Pearl, C., Platnick, S., Poulsen, C., Riedi, J., Sun-Mack, S., Walther, A., Winker, D., Zeng, S., and Zhao, G.: Assessment of Global Cloud Datasets from Satellites: Project and Database Initiated by the GEWEX Radiation Panel, *B. Am. Meteorol. Soc.*, 94, 1031–1049, <https://doi.org/10.1175/BAMS-D-12-00117.1>, 2013.
- Sturm, M., Holmgren, J., König, M., and Morris, K.: The thermal conductivity of seasonal snow, *J. Glaciol.*, 43, 26–41, <https://doi.org/10.3189/S0022143000002781>, 1997.
- Swart, N. C., Cole, J. N. S., Kharin, V. V., Lazare, M., Scinocca, J. F., Gillett, N. P., Anstey, J., Arora, V., Christian, J. R., Hanna, S., Jiao, Y., Lee, W. G., Majaess, F., Saenko, O. A., Seiler, C., Seinen, C., Shao, A., Sigmund, M., Solheim, L., von Salzen, K., Yang, D., and Winter, B.: The Canadian Earth System Model version 5 (CanESM5.0.3), *Geosci. Model Dev.*, 12, 4823–4873, <https://doi.org/10.5194/gmd-12-4823-2019>, 2019.
- Swart, N. C., Cole, J., Kharin, S., Lazare, M., Scinocca, J., Gillett, N., Anstey, J., Arora, V., Christian, J., Hanna, S., Jiao, Y., Lee, W., Majaess, F., Saenko, O., Seiler, C., Seinen, C., Shao, A., Solheim, L., von Salzen, K., Yang, D., and Winter, B.: The Canadian Earth System Model (CanESM) – v5.0.3 (v5.0.3), Zenodo, <https://doi.org/10.5281/zenodo.3251114>, 2023.
- Tabler, R., Benson, C., Santana, B., and Ganguly, P.: Estimating snow transport from wind speed records: estimates versus measurements at Prudhoe Bay, Alaska, in: 58th Annual Western Snow Conference, Proceedings of the 58th Annual Western Snow Conference, 17–19 April 1990, Sacramento, California, Western Snow Conference, <https://westernsnowconference.org/sites/westernsnowconference.org/PDFs/1990Tabler.pdf> (last access: 14 September 2023), 1990.
- Taylor, K. E., Stouffer, R. J., and Meehl, G. A.: An Overview of CMIP5 and the Experiment Design, *B. Am. Meteorol. Soc.*, 93, 485–498, <https://doi.org/10.1175/BAMS-D-11-00094.1>, 2011.

- Tesdal, J.-E., Christian, J. R., Monahan, A. H., and von Salzen, K.: Evaluation of diverse approaches for estimating sea-surface DMS concentration and air-sea exchange at global scale, *Environ. Chem.*, 13, 390–412, <https://doi.org/10.1071/EN14255>, 2016a.
- Tesdal, J.-E., Christian, J. R., Monahan, A. H., and von Salzen, K.: Sensitivity of modelled sulfate aerosol and its radiative effect on climate to ocean DMS concentration and air-sea flux, *Atmos. Chem. Phys.*, 16, 10847–10864, <https://doi.org/10.5194/acp-16-10847-2016>, 2016b.
- Verseghy, D.: CLASS – The Canadian Land Surface Scheme (Version 3.6), Tech. rep., Environment Canada, 2012.
- Verseghy, D. L.: CLASS: A Canadian land surface scheme for GCMS. I. Soil model, *Int. J. Climatol.*, 11, 111–133, <https://doi.org/10.1002/joc.3370110202>, 1991.
- Verseghy, D. L., McFarlane, N. A., and Lazare, M.: A Canadian land surface scheme for GCMs: II Vegetation model and coupled runs., *Int. J. Climatol.*, 13, 347–370, 1993.
- Virgin, J. G., Fletcher, C. G., Cole, J. N. S., von Salzen, K., and Mitovski, T.: Cloud Feedbacks from CanESM2 to CanESM5.0 and their influence on climate sensitivity, *Geosci. Model Dev.*, 14, 5355–5372, <https://doi.org/10.5194/gmd-14-5355-2021>, 2021.
- von Salzen, K., Scinocca, J. F., McFarlane, N. A., Li, J., Cole, J. N. S., Plummer, D., Verseghy, D., Reader, M. C., Ma, X., Lazare, M., and Solheim, L.: The Canadian Fourth Generation Atmospheric Global Climate Model (CanAM4). Part I: Representation of Physical Processes, *Atmosphere-Ocean*, 51, 104–125, <https://doi.org/10.1080/07055900.2012.755610>, 2013.
- Webb, M. J., Andrews, T., Bodas-Salcedo, A., Bony, S., Bretherton, C. S., Chadwick, R., Chepfer, H., Douville, H., Good, P., Kay, J. E., Klein, S. A., Marchand, R., Medeiros, B., Siebesma, A. P., Skinner, C. B., Stevens, B., Tselioudis, G., Tsushima, Y., and Watanabe, M.: The Cloud Feedback Model Intercomparison Project (CFMIP) contribution to CMIP6, *Geosci. Model Dev.*, 10, 359–384, <https://doi.org/10.5194/gmd-10-359-2017>, 2017.
- Wild, M.: The global energy balance as represented in CMIP6 climate models, *Clim. Dynam.*, 55, 553–577, <https://doi.org/10.1007/s00382-020-05282-7>, 2020.
- Wood, R.: Drizzle in Stratiform Boundary Layer Clouds. Part II: Microphysical Aspects, *J. Atmos. Sci.*, 62, 3034–3050, <https://doi.org/10.1175/JAS3530.1>, 2005.
- Wu, K., Li, J., von Salzen, K., and Zhang, F.: Explicit solutions to the mixing rules with three-component inclusions, *J. Quant. Spectrosc. Ra.*, 207, 78–82, <https://doi.org/10.1016/j.jqsrt.2017.12.020>, 2018.
- Yang, P., Bi, L., Baum, B. A., Liou, K.-N., Kattawar, G. W., Mishchenko, M. I., and Cole, B.: Spectrally Consistent Scattering, Absorption, and Polarization Properties of Atmospheric Ice Crystals at Wavelengths from 0.2 to 100 μm , *J. Atmos. Sci.*, 70, 330–347, <https://doi.org/10.1175/JAS-D-12-039.1>, 2012.
- Zelinka, M. D., Myers, T. A., McCoy, D. T., Po-Chedley, S., Caldwell, P. M., Ceppi, P., Klein, S. A., and Taylor, K. E.: Causes of Higher Climate Sensitivity in CMIP6 Models, *Geophys. Res. Lett.*, 47, e2019GL085782, <https://doi.org/10.1029/2019GL085782>, 2020.
- Zelinka, M. D., Klein, S. A., Qin, Y., and Myers, T. A.: Evaluating Climate Models' Cloud Feedbacks Against Expert Judgment, *J. Geophys. Res.-Atmos.*, 127, e2021JD035198, <https://doi.org/10.1029/2021JD035198>, 2022.
- Zhang, Y., Carey, S. K., and Quinton, W. L.: Evaluation of the algorithms and parameterizations for ground thawing and freezing simulation in permafrost regions, *J. Geophys. Res.-Atmos.*, 113, D17116, <https://doi.org/10.1029/2007JD009343>, 2008.
- Zhao, L. and Gray, D. M.: A parametric expression for estimating infiltration into frozen soils, *Hydrol. Process.*, 11, 1761–1775, [https://doi.org/10.1002/\(SICI\)1099-1085\(19971030\)11:13<1761::AID-HYP604>3.0.CO;2-O](https://doi.org/10.1002/(SICI)1099-1085(19971030)11:13<1761::AID-HYP604>3.0.CO;2-O), 1997.
- Zhou, C., Zelinka, M. D., and Klein, S. A.: Analyzing the dependence of global cloud feedback on the spatial pattern of sea surface temperature change with a Green's function approach, *J. Adv. Model. Earth Sy.*, 9, 2174–2189, <https://doi.org/10.1002/2017MS001096>, 2017.
- Zhou, T., Turner, A. G., Kinter, J. L., Wang, B., Qian, Y., Chen, X., Wu, B., Wang, B., Liu, B., Zou, L., and He, B.: GM-MIP (v1.0) contribution to CMIP6: Global Monsoons Model Inter-comparison Project, *Geosci. Model Dev.*, 9, 3589–3604, <https://doi.org/10.5194/gmd-9-3589-2016>, 2016.
- Zobler, L.: A World Soil File for Global Climate Modelling, Tech. Rep. NASA Technical Memorandum 87802, NASA Goddard Institute for Space Studies, New York, New York, USA, 1986.